

The initial mass-final luminosity relation of type II supernova progenitors. Hints of new physics?

OSCAR STRANIERO,^{1,2} INMA DOMINGUEZ,³ LUCIANO PIERSANTI,¹ MAURIZIO GIANNOTTI,⁴ AND ALESSANDRO MIRIZZI^{5,6}

¹*Istituto Nazionale di Astrofisica, Osservatorio d'Abruzzo, Via Maggini s.n.c., 64100, Teramo, IT*

²*Istituto Nazionale di Fisica Nucleare, Laboratori Nazionali del Gran Sasso, IT*

³*Departamento de Física Teórica y del Cosmos, Universidad de Granada, 18071 Granada, ES*

⁴*Physical Sciences, Barry University, 11300 NE 2nd Ave., Miami Shores, FL 33161, USA*

⁵*Dipartimento Interateneo di Fisica "Michelangelo Merlin", Via Amendola 173, 70126 Bari, IT*

⁶*Istituto Nazionale di Fisica Nucleare, Sezione di Bari, IT*

(Received; Revised; Accepted July 16, 2019)

Submitted to ApJ

ABSTRACT

We revise the theoretical initial mass-final luminosity relation for progenitors of type IIP and IIL supernovae. The effects of the major uncertainties, as those due to the treatment of convection, semiconvection, rotation, mass loss, nuclear reaction rates and neutrinos production rates are discussed in some details.

The effects of mass transfer between components of close-binary systems are also considered. By comparing the theoretical predictions to a sample of type II supernovae for which the initial mass of the progenitors and the pre-explosive luminosity are available, we conclude that stellar rotation may explain a few progenitors which appear brighter than expected in case of non-rotating models. In the most extreme case, SN2012ec, an initial rotational velocity up to 300 km s⁻¹ is required. Alternatively, these objects could be mass-losing components of close binaries. However, most of the observed progenitors appear fainter than expected. This occurrence seems to indicate that the Compton and pair neutrino energy-loss rates, as predicted by the standard electro-weak theory, are not efficient enough and that an additional negative contribution to the stellar energy balance is required. We show that axions coupled with parameters accessible to currently planned experiments, such as IAXO and, possibly, Baby-IAXO and ALPS II, may account for the missing contribution to the stellar energy-loss.

Keywords: astroparticle physics — stars: evolution: stars: massive — stars: rotation — supernovae: general

1. INTRODUCTION

The progenitors of type II supernovae (SNe) are massive stars that retain part of their H-rich envelope up to the onset of the core collapse. Recent surveys devoted to the search of type II progenitors, found that the majority of the supernovae of this class observed in the local Universe, those of type IIP (plateau) and type IIL (linear), are produced by red supergiants (RSG) whose luminosity never exceeds $\log L/L_{\odot} = 5.1$ (see the recent review by Smartt 2015). According to current massive star models, such a pre-explosive luminosity corresponds to an initial mass¹ of about 16 - 18 M_⊙, with some differences from author to author, depending on the adopted treatment of convective mixing and/or the initial rotational velocity (Limongi et al. 2000; Woosley et al. 2002; Hirschi et al. 2004; Eldridge & Tout 2004; Woosley & Heger 2007; Georgy et al. 2013; Farmer et al. 2016; Limongi & Chieffi 2018). This occurrence is at odd with an early theoretical suggestion for which a type II supernova is expected to be the final fate of red supergiants with initial mass up to $\sim 30 M_{\odot}$ (e.g., Woosley & Heger 2007). Several solutions of this puzzling problem have been

Corresponding author: Oscar Straniero
oscar.straniero@inaf.it

¹ With *initial mass* we intend the mass at the zero-age-main-sequence (ZAMS) or, equivalently, the mass at the beginning of the H-burning phase.

proposed (Smartt 2015), among which observational biases or higher mass-loss rate for the more massive and brighter progenitors, which eventually explode as SNe of other types. Alternatively, it is possible that for stars with initial mass $M > 18 M_{\odot}$ the core collapse is not followed by a SN explosion. In these *failed-supernova* scenario, the energy deposited by neutrinos may be not enough to sustain the forward shock, thus leading to the formation of a black hole. Recent parametric studies of core-collapse models have investigated the conditions for which a star can (or can not) explode (O’Connor & Ott 2011; Ugliano et al. 2012; Horiuchi et al. 2014; Pejcha & Thompson 2015; Sukhbold et al. 2016; Ertl et al. 2016; Ebinger et al. 2019). They found that there is not a single mass below which all stars explode. Rather, there are islands of “explodability”, separated by regions of progenitor masses corresponding to non-exploding models. In general, it appears that 95% of type II supernovae should have initial masses $9 < M/M_{\odot} < 22$. Successful explosions are obtained for the majority of the models within this mass range. Type II supernovae with initial mass between 25 and 27 M_{\odot} are also possible, while models in the range 22 and 25 M_{\odot} and between 27 and 30 M_{\odot} in most cases collapse into black holes, directly or by fall back. Eventually, stars whose initial mass is above 30 M_{\odot} lose their H-rich envelope before the final collapse and may give rise to type Ib or Ic supernovae². In summary, the picture arising from these theoretical studies is much more challenging and rich than the simple scenario derived from the few observations of RSG progenitors available so far. Nonetheless, the lack of RSG progenitors more massive than 18 M_{\odot} still appears in conflict with the theoretical expectation.

Two alternative methods to estimate the progenitor masses have been recently developed (Utrobin & Chugai 2009; Spiro et al. 2014; Jerkstrand et al. 2014; Barbarino et al. 2015; Valenti et al. 2016; Morozova et al. 2018). The first is based on the best fit of the observed SN light curve, which provides information about the mass of the exploding stars and of the dense circumstellar material supposed to be the result of the progenitor stellar wind. According to Morozova et al. (2018), the progenitor masses estimated with this method range between 10.9 and 22.9 M_{\odot} (95% C.L.) and are consistent with a Salpeter’s mass distribution. The upper mass bound, in particular, is substantially larger than that obtained by means of the pre-explosive luminosities and in a better agreement with the theoretical expectations. The second method makes use of late-time spectra (nebular phase) to measure the oxygen yield of the supernova. Oxygen is a product of the hydrostatic nucleosynthesis and depends on the progenitor mass. Also in this case, the resulting masses are generally larger than those estimated by means of the pre-explosive luminosity (see Figure 7 in Davies & Beasor 2018, and section 4).

Motivated by this mass discrepancy, in this work we have investigated possible revisions of the current scenario of massive star evolution that might imply a variation of the pre-explosive luminosity of red supergiant progenitors of type II SNe. In the next section we revise the standard scenario, discussing the uncertainties affecting massive star models with mass ranging between 11 and 30 M_{\odot} . Then, in section 3 we discuss a possible *new-physics* solution. Specifically, we show that axions or axion-like particles (ALPs), whose couplings with photons and electrons are compatible with current bounds and accessible to the next generation of experiments, could be efficiently produced in the stellar cores of massive stars, thus leading to an increase of the energy-loss rate. A summary of our conclusions follows. Numerical expressions for the axion rates used in this work and some additional discussion about their relevance for different plasma conditions are illustrated in the appendix.

2. STANDARD MODELS

In this section we review the current massive star models and the physical processes which determine their final luminosity. We will make use of models computed by other groups and available in the extant literature, and of a new set of models specially computed by means of the Full Network Stellar evolution code (FuNS, Straniero et al. 2006; Piersanti et al. 2013). Let us first summarize the main features of this code.

2.1. The FuNS code

The solver we use to integrate the differential equations describing the stellar equilibrium structure and the chemical evolution is based on a classical Henyey method. It was originally derived from the former FRANEC code (Chieffi & Straniero 1989). The last version of the FuNS allows us to choose different degrees of coupling between the equations describing the physical structure and those describing the chemical evolution, as due to nuclear burning and mixing. For the models discussed in this work, we have adopted a scheme in which the stellar structure equations (i.e., hydrostatic equilibrium, mass continuity, energy conservation and energy transport) and the chemical evolution equations due to

² In case of mass loss driven by Roche-lobe overflow in a close binary system, the mass of a SNe Ib/Ic progenitor can be smaller

the nuclear burning are solved simultaneously. Then, the stellar zones which are thermally unstable are separately mixed. When dealing with the advanced stages of the evolution of a massive star, such a scheme is a good compromise between accuracy, velocity and stability of the numerical solutions. Our code also allows three different choices of the time dependent mixing scheme, namely: diffusive, advective or the non-local algorithm described in [Straniero et al. \(2006\)](#). For the purpose of this paper the three schemes are equivalent. In order to calculate the temperature gradient and the average turbulent velocity (or diffusion coefficient) in the convective regions we use, as usual, the mixing length theory. In particular, we follow the scheme described in [Cox & Giuli \(1968\)](#). The mixing length parameter (α_{ML}) has been calibrated by means of a Standard Solar Model ([Piersanti et al. 2007](#)). Note that the value of α_{ML} depends on the adopted solar composition. Since we adopt the [Lodders et al. \(2009\)](#) composition, we found $\alpha_{ML} = 1.9$.

In general, the convective boundaries are fixed according to the Ledoux criterion (see section 2.2). In addition, during the He-burning phase, the external border of the convective core is found by imposing the condition of marginal stability, i.e., ∇_{rad} strictly equal to ∇_{ad} (for more details see [Straniero et al. 2003](#)). Except for the models described in section 2.3, no convective overshoot is applied.

The FuNS code also account for stellar rotation ([Piersanti et al. 2013](#)). As usual, we assume shellular rotation, i.e., constant angular velocity and composition on the isobaric surfaces (see, e.g., [Maeder 2009](#)). As illustrated in section 2.4, the most important instabilities induced by rotation, which are responsible for transport of angular momentum and mixing, are considered. The potential effects of the magnetic field on rotation are ignored.

The FuNS has been optimized to handle large nuclear networks, as those required to follow the neutron-capture nucleosynthesis in AGB stars (see [Straniero et al. 2006](#)). However, a minimal nuclear network that includes all the reactions providing the major contribution to the energy production is enough for the purpose of the present paper and allows to reduce the computational time consumption. Hence, we have considered 33 isotopes, from ^1H to ^{56}Ni , coupled by 19 reactions for the H burning (those describing a full pp-chain and CNO-cycle) and an α -chain of 51 reactions, plus the $^{12}\text{C}+^{12}\text{C}$, $^{12}\text{C}+^{16}\text{O}$ and $^{16}\text{O}+^{16}\text{O}$, for the more advanced burnings. The reaction rates are from the STARLIB database ([Sallaska et al. 2013](#)). Most of the H and He burning reaction rates in this database are based on available experimental data. Rate estimates of reactions for which no experimental information exists, or extrapolation to low temperatures at which no experimental rates exist, are obtained by means of statistical (HauserFeshbach) models of nuclear reactions, computed using the code TALYS ([Goriely et al. 2008](#)). Finally, electron screening corrections are computed according to [Dewitt et al. \(1973\)](#); [Graboske et al. \(1973\)](#); [Itoh et al. \(1979\)](#). Other details on the FuNS input physics are here provided:

- Neutrino Energy Loss:
 - Plasma – [Haft et al. \(1994\)](#)
 - Photo – [Itoh et al. \(1996a\)](#)
 - Pair – [Itoh et al. \(1996a\)](#)
 - Bremsstrahlung – [Dicus et al. \(1976\)](#)
 - Recombination – [Beaudet et al. \(1967\)](#)
- Radiative Opacity:
 - [Alexander & Ferguson \(1994\)](#)+[Iglesias & Rogers \(1996\)](#)+[Magee et al. \(1995\)](#)
- Electron Conductivity:
 - [Potekhin et al. \(1999\)](#); [Potekhin \(1999\)](#)
- Equation of State:
 - [Rogers et al. \(1996\)](#) + [Straniero \(1988\)](#) (see also [Prada Moroni & Straniero 2002](#))
- Mass Loss:
 - [Nieuwenhuijzen & de Jager \(1990\)](#)
- External Boundary Conditions:

Table 1. Initial Mass of type II SN progenitors with final luminosity $\log L/L_{\odot} = 5.1$.

Name	M/M _⊙	Reference
Standard non-rotating Models		
FuNS	18.9	present work
KEPLER	18.5	Woosley et al. (2002)
with convective overshoot		
$\beta = 0.01$	17.0	present work
$\beta = 0.02$	13.8	present work
GENEVA	18.9	Meynet et al. (2015)
MESA	18.9	Farmer et al. (2016)
ORFEO	17.4	Limongi & Chieffi (2018)
STARS	15.6	Eldridge & Tout (2004)
with different compositions		
Y=0.32 Z=0.014	17.6	present work
Y=0.27 Z=0.006	17.7	present work
with rotation		
$v_{ini} = 200 \text{ km s}^{-1}$	11.8	present work
$v_{ini} = 150 \text{ km s}^{-1}$	13.0 ^a	Limongi & Chieffi (2018)
$v_{ini} = 0.4v_{crit}$	17.1	Meynet et al. (2015)
with axion energy loss		
$g_{10} = 0.6, g_{13} = 0$	19.8	present work
$g_{10} = 0.6, g_{13} = 4$	20.9	present work

^aIt is a blue supergiant

– scaled solar $T(\tau)$ relation (Krishna Swamy 1966)

As it is well known, the luminosity of a red supergiant and its He-core mass are closely related. Indeed, the mass of the core determines the physical conditions (T and ρ) of the H-burning shell, which is the source of energy that sustains the shining of these stars. After the He-burning phase, the central temperature rapidly increases becoming larger than $\sim 5 \times 10^8$ K. At that temperatures, the production of neutrinos, as due to the Compton scattering and e^+e^- annihilation, becomes very efficient. As a result, the advanced stages of the evolution of a massive star are controlled by the neutrino energy loss that largely overcomes the photon energy loss. Such an occurrence causes a rapid drop of the evolutionary time scale, which becomes much smaller than the H-burning time scale. Hence, since the exhaustion of the central carbon and until the final collapse, the He-core mass and, in turn, the stellar luminosity stop to grow. In the rest of this section we will review the most important physical processes that determine the growth of the He-core mass up to this constant value and, hence, their impact on the pre-explosive luminosity.

The new models here presented have masses between 11 and 30 M_{\odot} . If not differently specified, we have assumed solar composition, i.e., $Z=0.014$ and $Y=0.27$. All the models, except those with $M = 11 M_{\odot}$, have been evolved up to the Si burning, when the central temperature is $\sim 4 \times 10^9$ K. Instead the calculation of the $M = 11 M_{\odot}$ models has been stopped just after the off-center Ne ignition.

2.2. Semiconvection

Among the principal uncertainties affecting H and He burning models of massive stars, those related to the treatment of turbulent mixing induced by convection still remain the most debated. In this context, a longstanding problem concerns the criterion adopted to establish if a not homogeneous zone is unstable against convection. In particular, in case of a negative molecular weight gradient, it may happens that a thermally unstable stratification is stabilized against adiabatic convection by a gradient in composition. This phenomenon, often called semiconvection, is particularly relevant for massive stars (see Langer et al. 1985). In this case, the widely adopted Schwarzschild criterion, which ignores the stabilizing effect of the molecular weight gradient, appears inadequate to model the mixing and the consequent heat transport. On the other hand, the Ledoux criterion, which includes composition effects, hampers mixing in semiconvective regions.

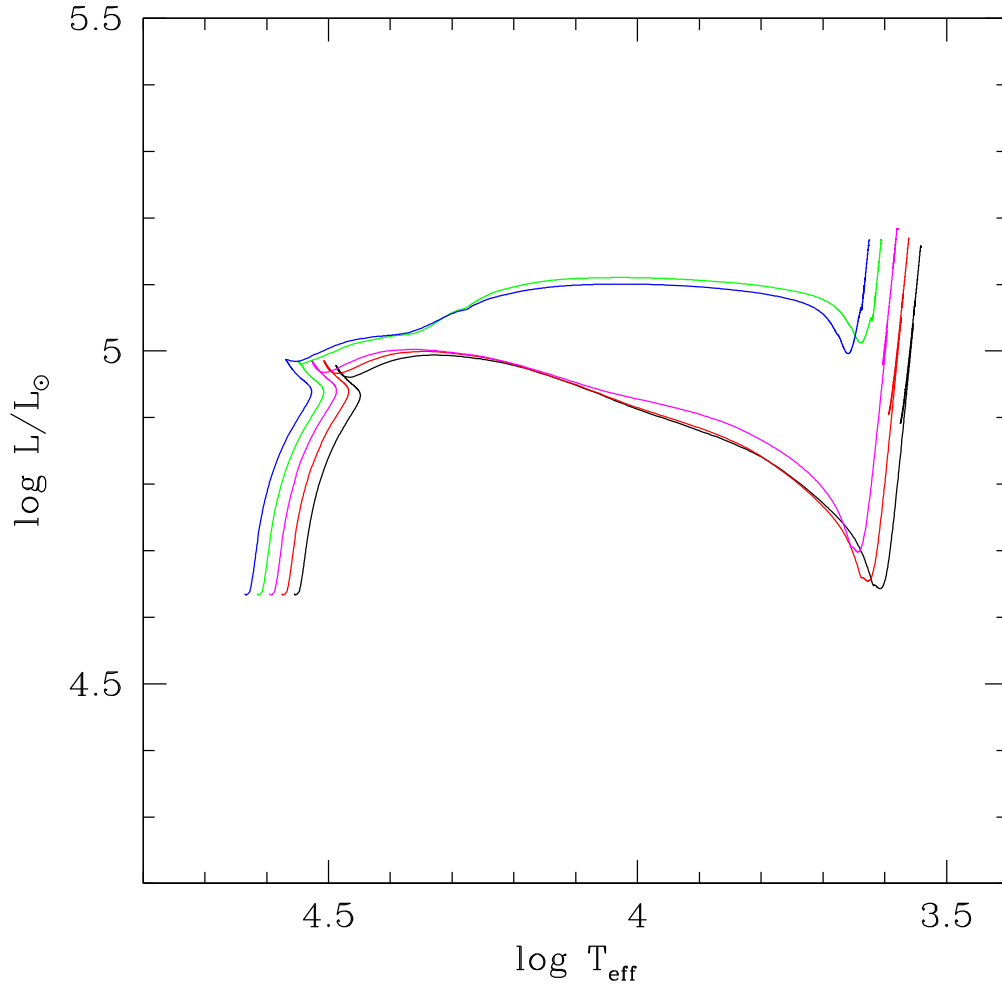


Figure 1. Evolutionary tracks of $20 M_{\odot}$ models as obtained under different assumptions about the mixing efficiency in the semiconvective zones (see text for details): $\eta = 10^{-3}$ (green), $\eta = 10^{-4}$ (blue), $\eta = 10^{-5}$ (magenta), $\eta = 10^{-6}$ (red), $\eta = 0$ (black). Note that, in order to distinguish the different models, relative shifts of $\Delta \log T_{\text{eff}} = 0.02$ have been applied to the tracks with $\eta > 0$.

Concerning massive stars, semiconvective zones firstly appear during the H-burning phase, when the convective core recedes, as a consequence of the conversion of H into He, and a region of negative μ gradient is left outside. If according to the Schwarzschild criterion these layers are efficiently mixed, a prompt He ignition occurs after the exhaustion of the central hydrogen, when the star is still a compact blue supergiant. Then, during most of the He-burning phase the star remains hot and only towards the end of this phase it eventually becomes a RSG. On the contrary, if according to the Ledoux criterion the mixing is inhibited in the semiconvective layers, after the central-H exhaustion the stellar envelope expands and the star directly evolves into a cool and red supergiant. In this case the He ignition takes place on the RSG branch.

A simple analysis of stability (see Kippenhahn & Weigert 1990) demonstrates that even if the normal convective modes are stable, oscillatory modes can exist that may induce some mixing in the semiconvective layers. On the other hand, observations of massive stars in the Milky Way and in the Magellanic Clouds clearly favor a prompt evolution to the red supergiant phase (Stothers & Chin 1992a, 1994). Figure 1 shows some evolutionary tracks of the models we obtained by varying the damping factor (η) of the semiconvective velocity (v_{sc}) with respect to the fully convective velocity (v_c). In practice, we have assumed that $v_{sc} = \eta v_c$ and varied the η parameter from 0 to 10^{-3} . Note that the case $\eta = 0$ corresponds to the bare Ledoux criterion, while for $\eta = 1$, the effect of the molecular weight gradient is

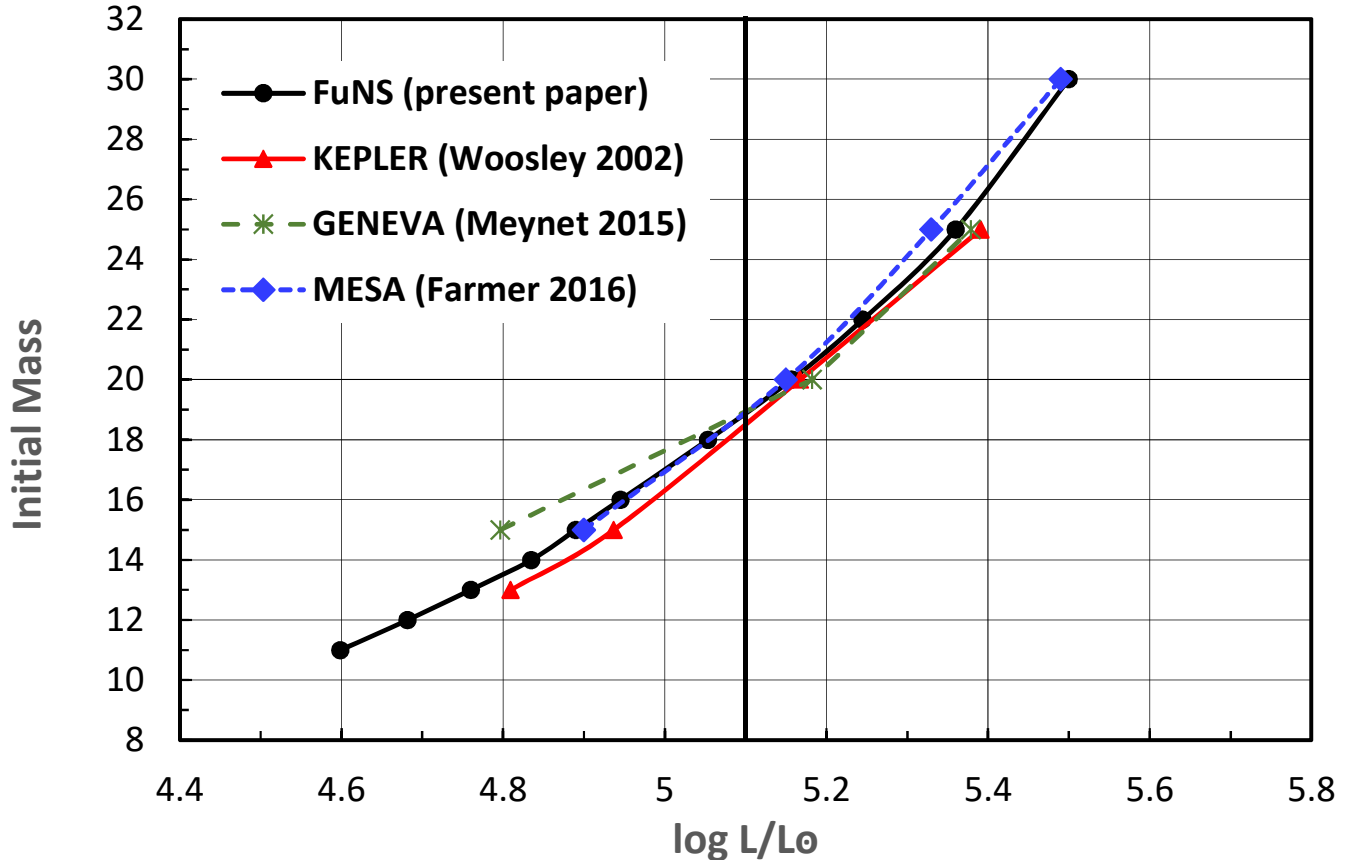


Figure 2. Initial mass-final luminosity relation for non-rotating stellar models. At the onset of the core collapse, all the models are red supergiants, except for the $25 M_{\odot}$ GENEVA model.

fully suppressed. Only models with $\eta \leq 10^{-5}$ become red supergiants before the He ignition. Note, however, that the variation of the final luminosity is rather small, namely $\Delta \log L < 0.03$. In the rest of the paper, we will adopt the Ledoux criterion. The resulting initial mass-final luminosity relation is reported in Figure 2. For comparisons, other relations, as obtained from non-rotating models with moderate or no overshoot, are also shown, namely KEPLER (Woosley et al. 2002), GENEVA (Meynet et al. 2015) and MESA (Farmer et al. 2016). The small differences are likely due to the adopted treatments of overshoot, semiconvection and mass loss. The vertical line marks the observed upper limit for the luminosity of type II SN progenitors (Smartt 2015). The corresponding masses are reported in Table 1.

2.3. Convective Overshoot

The so-called convective-core overshoot is another phenomenon that may affect the final He-core mass and, in turn, the final luminosity of a massive star. Indeed, owing to the inertial motion of the convective cells, a transition zone, rather than a sharp discontinuity, should exist between stable and unstable regions. In principle, the extension of this zone and the mixing efficiency within it depend on the convective velocity at the boundary layer and on the steepness of the entropy gradient. Therefore, a unique prescription to be applied to all the convective boundaries appears unrealistic. In most cases hints on the overshooting extension may be provided by the observations of the stellar properties affected by this phenomenon. Concerning massive stars, Stothers & Chin (1992b) (but see also Maeder & Meynet 1989) have shown that the convective-core overshoot cannot be too large, otherwise it would be in conflict with observations. Nevertheless, in order to quantify the effect of this phenomenon on the initial mass-final luminosity relation, we have computed two additional set of models with convective-core overshoot. In practice, according to current hydrodynamical simulations of stellar convection (see, e.g., Freytag et al. 1996), we have extended the mixing outside the fully convective core of the H-burning models by imposing an exponential decline of the convective velocity,

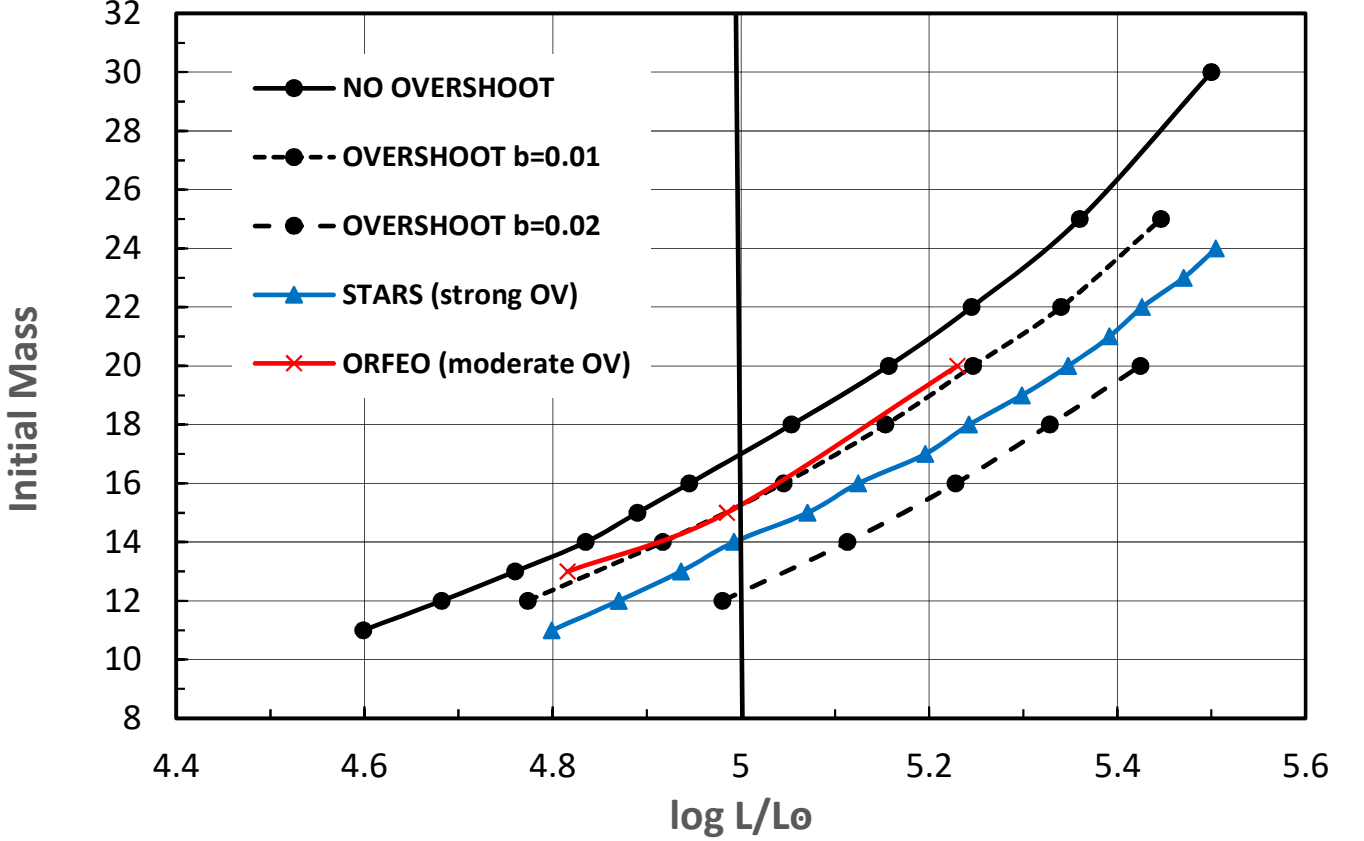


Figure 3. Initial mass-final luminosity relation from FuNS models with convective overshoot. For comparisons, the FuNS standard relation (no overshoot) and those derived from models of other authors are also shown (see text for references).

namely:

$$v_{ov} = v_{cct} \exp\left(-\frac{\delta r}{\beta H_p}\right) \quad (1)$$

where v_{cct} is the convective velocity at the top of the fully convective core³, δr is the radial distance from the convective border and H_p is the pressure scale height. β is a free parameter. The results are shown in Figure 3 for $\beta = 0.01$ and 0.02 , short- and long-dashed lines, respectively. For a given stellar mass, the final He-core mass is larger in case of convective overshoot and, in turn, the pre-explosive models are brighter than those obtained by neglecting the overshoot mixing (solid line). For comparison, we have also reported the initial mass-final luminosity relations from two extant set of stellar models with overshoot, namely: ORFEO (Limongi & Chieffi 2018) and STARS (Eldridge & Tout (2004)⁴. Note that a moderate overshoot (of the order of $0.1H_p$) has been adopted in the ORFEO models, while the extra-mixing zone is rather extended in STAR models ($\sim 0.5H_p$). The corresponding upper mass bounds for the observed progenitors of type II supernovae are also listed in Table 1. In case of large overshoot, this maximum mass would be particularly small, thus increasing the tension with the masses estimated by means of light curve best fitting or from the oxygen yields measured in the nebular phase. (Morozova et al. 2018; Davies & Beasor 2018). In addition, due to the higher luminosity, the mass-loss is larger in models with convective-core overshoot. As a result, also the maximum mass of collapsing red supergiants is smaller than that predicted by models without overshoot.

2.4. Rotation

Rotational velocity of the order of $100\text{-}200 \text{ km s}^{-1}$ are commonly observed in main sequence massive stars (Hunter et al. 2008). As it is well known, 1D hydrostatic codes may easily account for shellular rotation (Endal & Sofia 1976).

³ This is the marginal stability border of the convective core, where $\nabla_{rad} = \nabla_{ad}$

⁴ As derived from Figure 4 in Smartt (2015).

Two are the major consequences of rotation, namely: i) the lifting due to the centrifugal force, and ii) the meridional circulation that arises because of the deviations from thermal equilibrium occurring in rotating structures (Von Zeipel's paradox). The lifting effect of rotation implies more expanded and cooler stellar structures. In addition, the mixing induced by meridional circulation modifies the mean molecular weight and the opacity of the envelope. As a result, larger convective core are expected in H and He burning stars with rotation. However, a quantitative estimation of these effects requires a reliable description of the angular momentum redistribution as due to both dynamical and secular instabilities. Moreover, angular momentum loss driven by stellar wind, which is particularly intense when the star is a red supergiant, must be considered.

In the present version of the FuNS code the transport of angular momentum is treated as a diffusive process (see details in Piersanti et al. 2013). The most important instabilities induced by rotation are considered. The Eddington-Sweet (ES) and, to a less extend, the Goffrei-Shubert-Fricke (GSF) instabilities may produce significant effects on the evolution of massive stars (Heger & Langer 2000). According to Kippenhahn & Weigert (1990) the ES circulation velocity is given by:

$$v_{ES} = \frac{\nabla_{ad}}{\delta(\nabla_{ad} - \nabla)} \frac{\omega^2 r^2 L}{(Gm)^2} \left(\frac{2\epsilon r^2}{L} - \frac{2r^2}{m} - \frac{3}{4\pi r^2 \rho} \right) \quad (2)$$

where, ω is the angular velocity, ϵ is the rate of energy loss per unit mass, $\delta = -\frac{\partial \ln \rho}{\partial \ln T}$, ∇ and ∇_{ad} are the temperature gradient and the adiabatic gradient, respectively. L , m , r , G and ρ have the usual meaning. As for convection, a negative molecular weight gradient reduces the efficiency of the meridional circulation. According to Kippenhahn (1974), we model the effect of the μ -gradient by defining an equivalent μ current, which works against the ES circulation:

$$v_{\mu} = f_{\mu} \frac{H_P}{\tau} \frac{\phi \nabla_{\mu}}{\nabla - \nabla_{ad}} \quad (3)$$

where H_P is the pressure scale height, $\phi = \frac{\partial \ln \rho}{\partial \ln \mu}$, $\nabla_{\mu} = \frac{\partial \ln \mu}{\partial \ln P}$ is the μ gradient and τ is the thermal relaxation timescale (also called Kelvin-Helmholtz timescale). f_{μ} is a (free) parameter used to tune the strength of the μ gradient barrier. Hence, the effective circulation velocity is: $|v_{MC}| = |v_{ES}| - |v_{\mu}|$. Such a velocity is used to calculate the angular momentum diffusion coefficient, while a fraction of it, i.e., $v_{rot} = f_c v_{MC}$, is used to calculate the mixing induced by rotation. In principle, both f_{μ} and f_c should vary between 0 and 1. These parameters could be calibrated by requiring that models reproduce some observables, such as the modification of the surface composition due to mixing induce by the meridional circulation (see, e.g., Heger & Langer 2000; Limongi & Chieffi 2018; Maeder 2009). Alternatively, asteroseismology may provide more stringent constraints to the efficiency of the angular momentum transport. Indeed, it allows to measure core rotation rates of stars in different evolutionary phases (see Eggenberger et al. 2019, and references therein). The first results of the application of this method, mainly concerning low- and intermediate-mass stars, seem to indicate that the angular momentum redistribution is very efficient. In general, this occurrence should reduce the effects of rotation. Unfortunately, a clear and unique prescription valid for massive stars is still lacking. This problem represents a further uncertainty affecting massive star models. In Figure 4 we report the evolutionary tracks of a 20 M_{\odot} star as obtained under different assumption about f_c , f_{μ} and the initial (uniform) rotational velocity (v_{ini}). In general, the final He-core mass is larger than that of non-rotating models. As a consequence, a rotating SN progenitor is brighter than a non-rotating one. However, the extent of this effect depends on the assumed set of rotation parameters.

In Figure 5, the variation of the initial mass-final luminosity relation for models with rotation is illustrated. The FuNS relation for $v_{ini} = 200 \text{ km s}^{-1}$, $f_c = 0.04$ and $f_{\mu} = 0$, is shown, together with that from the ORFEO database (Limongi & Chieffi 2018, $v_{ini} = 150 \text{ km s}^{-1}$, $f_c = 1$ and $f_{\mu} = 0.05$), and that from the GENEVA code (Meynet et al. 2015, $v_{ini} = 0.4v_{crit}$). Note that a spread of v_{ini} implies a spread of the final luminosity. In other words, an observed pre-explosive luminosity do not correspond to a unique value of the initial mass. Instead a range of masse is possible, depending on the (unknown) initial rotational velocity.

Another important consequence of rotation concerns the mass loss (Meynet et al. 2015). Indeed, owing to the higher luminosity, the mass-loss rate is larger in rotating models. As a result, we find that rotating models ($v_{ini} = 200 \text{ km/s}$) whose initial mass is $M \geq 15 M_{\odot}$ leave the RSG branch before the final core collapse and, for this reason, they cannot be progenitors of type IIP/L SNe.

2.5. Mass loss

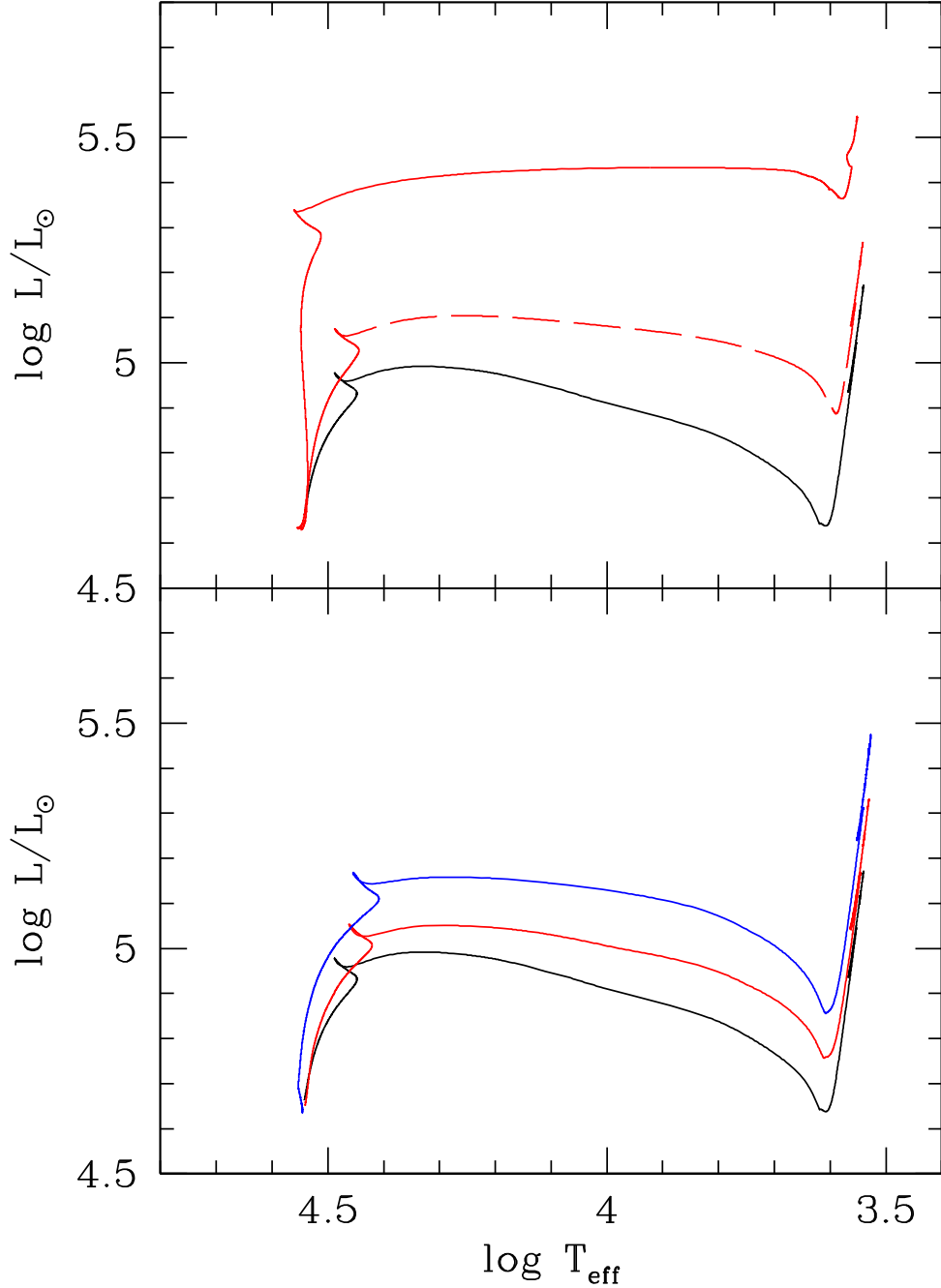


Figure 4. Evolutionary tracks of rotating models ($M=20 M_{\odot}$, no mass loss) for different sets of v_{ini} , f_c , f_{μ} . Upper panel: 100, 0.04, 0 (red-dashed line); 200, 0.04, 0 (red-solid line). Lower panel: 200, 1, 0.01 (red-solid line); 200, 1, 0.005 (blue-solid line). For comparisons, the non-rotating track is also reported (the black line in both panels).

The effect of the mass loss on the evolution of massive stars has been deeply investigated by several authors (for a detailed analysis of the mass loss effects see [Meynet et al. 2015](#)). The total amount of mass lost before the final collapse depends on the initial mass, the initial rotation velocity and the extension of the convective-core overshoot. For instance, basing on non-rotating FuNS models, a $13 M_{\odot}$ star loses less than $2 M_{\odot}$, while a $25 M_{\odot}$ is expected to lose about half of its initial mass. In general, this theoretical prediction is in good agreement with the observed mass ejecta of SN IIP progenitors ([Morozova et al. 2018](#)). As mentioned in the previous section, the higher RSG luminosity

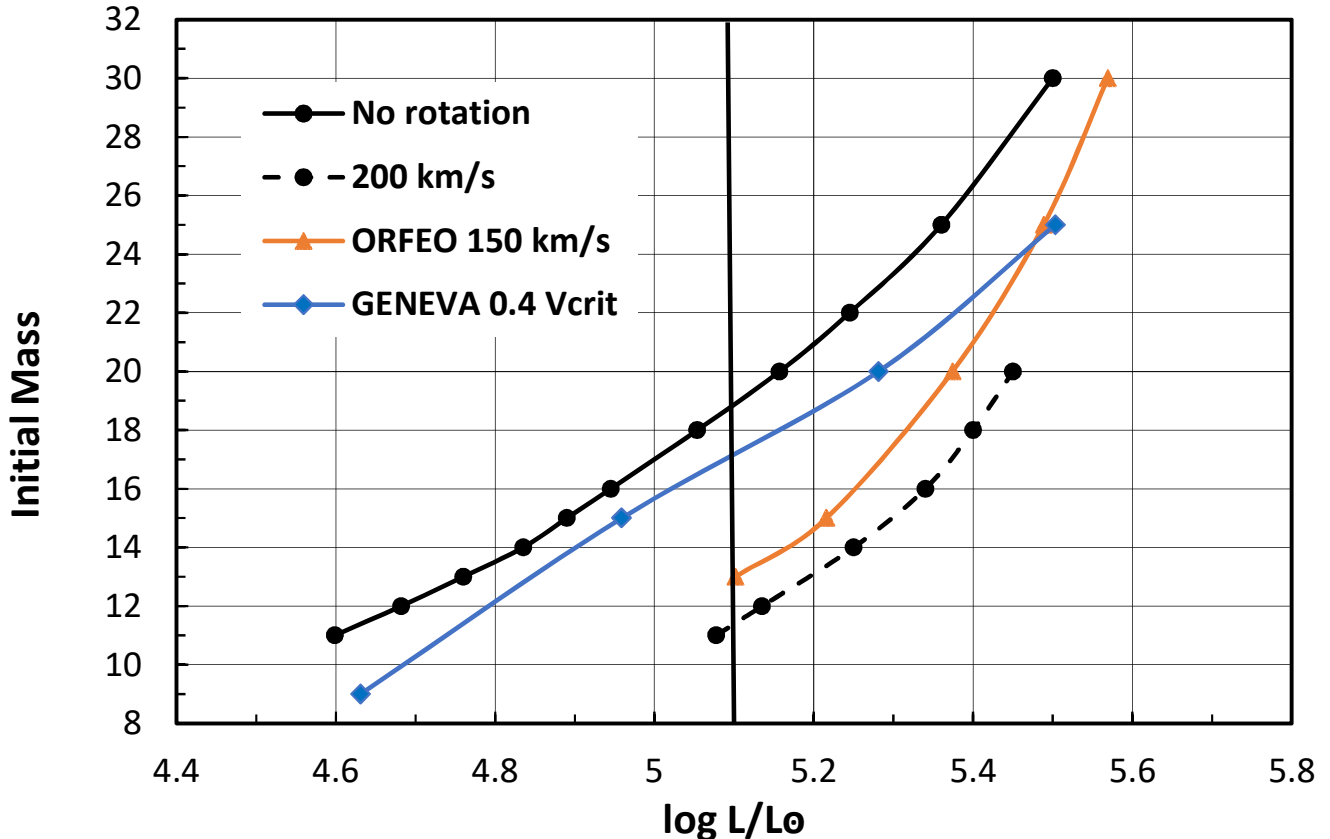


Figure 5. Initial mass-final luminosity relation for models with rotation (see text for references). Note that the FuNS rotating models with $M \geq 15 M_{\odot}$ leave the RSG branch before the occurrence of the core collapse. In contrast, none of the ORFEO models ends its evolution as red supergiant, while for the GENEVA rotating models the more massive pre-explosive RSG should have a mass between 15 and $20 M_{\odot}$. The vertical line at $\log L/L_{\odot} = 5.1$ marks the upper limit of the observed pre-explosive luminosities (according to Smartt 2015).

developed in case of rotation implies a stronger mass-loss rate. For the same reason, also models with convective overshoot develop higher mass-loss rate. In general, the larger the mass-loss rate the lower the final luminosity. We find, however, that the final luminosity does not depend on the mass lost during the RSG phase, but mostly on the amount of mass lost during the main sequence (see also section 2.9). Therefore, since the mass-loss rate is much lower in MS than in the RSG branch, the sensitivity of the initial mass-final luminosity on the adopted mass-loss rate is rather small. For instance, we find that in a non-rotating model of $18 M_{\odot}$ with mass loss, the final luminosity is only the 5% lower than that of a model without mass loss.

On the other hand, if the RSG mass loss is strong enough to erode the H-rich envelope, the model leaves the RSG branch prior to the final core collapse and the resulting supernova cannot be of type IIP/IIL. This occurrence implies a maximum RSG mass-loss rate for a progenitor of these SN types.

In this context, recent evidences of late time enhanced mass loss in progenitors of some bright SNe IIP/IIL (Moriya et al. 2011; Morozova et al. 2017; Yaron et al. 2017) are not expected to modify the initial mass-final luminosity relation for these stars. However, to explain pre-explosive outbursts commonly observed in SNe IIn, Fuller (2017) have recently suggested that gravity waves generated by vigorous convection during late-stage nuclear burning could transport energy upward, causing a heating of the H-rich envelope and, in turn, an increase of the final luminosity. Although firm conclusions about the occurrence and, eventually, the strength of such a heating process in normal SN IIP progenitors have not been established yet, we may exclude that it could solve the discrepancy between the masses estimated from the SN light curve and those derived from the pre-explosive luminosity. On the contrary, this phenomenon would increase the tension. Indeed, the masses from light curves are usually larger than those estimated from the initial mass-final luminosity relation (see the discussion in section 4).

2.6. Neutrinos

The rate of neutrino energy loss determines the time at which the evolutionary time scale becomes so short that the He-core mass stops to grow and a luminosity freeze-out occurs. In particular, a rate larger than that commonly estimated would imply fainter SN II progenitors. The current rates are computed on the base of the Weinberg-Salam electro-weak theory (see, e.g., Raffelt 1996). In the last 30 years, precision experiments have tested this quantum field theory at the level of one percent or better. Note, however, that the neutrino rates depend on the Weinberg angle, whose value is not predicted by the electro-weak theory. In the present calculations we have used the value suggested by Itoh et al. (1996a), namely: $\sin^2 \theta_W = 0.2319$, which is very similar to that reported in the latest compilation of the Particle Data Group⁵ (0.23155). We have also verified that negligible variations of the final luminosity are obtained when the CODATA 2014 value (0.2223, Mohr et al. 2016) is adopted. As a whole, the accuracy of the Compton and Pair neutrinos energy-loss rates, which are the dominant neutrinos processes in the present stellar model calculations, is better than 5% (Itoh et al. 1996a,b). Such an uncertainty has little effects on the pre-explosive luminosity.

On the other hand, some deviations from the standard electro-weak theory are not completely excluded. In particular, the existence of a non-zero neutrino magnetic moment would enhance the stellar energy-loss. Experimental and astrophysical constraints provide upper bounds for this quantity. The more stringent experimental constraint is $< 2.9^{-11} \mu_B$. It has been obtained by means of reactor neutrinos (90% C.L., Beda et al. 2013). A more stringent astrophysical constraint, as based on the luminosity of the RGB tip of Galactic Globular Clusters, gives $< 2.6^{-12} \mu_B$ (68% C.L., Viaux et al. 2013a). The influence of a non-zero neutrino magnetic moment on the evolution of massive stars has been investigated by Heger et al. (2009). They found that models of initial mass above $15 M_\odot$ are practically insensitive to a neutrino magnetic moment lower than $10^{-11} \mu_B$. However, they do not consider the sensitivity of the final luminosity on the enhanced neutrino rate. Therefore, we have computed a model of $20 M_\odot$ by assuming $\mu_\nu = 5 \times 10^{-11} \mu_B$ and we find that the resulting final luminosity is just a 2% lower than that of the corresponding $\mu_\nu = 0$ model.

2.7. Nuclear reaction rates

Similarly to neutrinos, also a variation of the C-burning temperature could anticipate or delay the time of the luminosity freeze-out. Indeed, owing to the strong sensitivity of the neutrino production rates on the temperature, a high C-burning temperature would anticipate the freeze-out, while the opposite occurs in case of a low C-burning temperature. This temperature depends on the rate of the $^{12}\text{C}+^{12}\text{C}$ reaction and on the amount of carbon left in the core after the He burning.

A large uncertainty affects the $^{12}\text{C}+^{12}\text{C}$ reaction rate for $T \leq 1$ GK (for a recent reanalysis, see Zickefoose et al. 2018, and references therein). At present, direct measurements of the cross section of this reaction are only available for energies > 2.1 MeV. Owing to a *molecular-like structure* of the ^{24}Mg compound nucleus, unknown resonances are possible at lower energy. The existence of these molecular states would substantially enhance the low-energy cross section, thus reducing the C-burning ignition temperature. In contrast, hindrance model (Jiang et al. 2007) predicts a steep drop of the low-energy $S(E)$ factor⁶ and, hence, would imply a larger C-burning ignition temperature. In this context, some hints may be obtained with indirect measurements. Tumino et al. (2018) have recently presented new results based the so-called Trojan Horse Method (THM). The THM is an indirect method, which allows to measure the $S(E)$ factors of charge particle reactions down to astrophysical relevant energies, where data from direct methods are not available because of the strong Coulomb barrier and the consequent very small cross sections. In the range of energy of more interest to the C-burning stellar rate, Tumino et al. found a complex resonant pattern, but no evidence of hindrance. However, the interpretation of these indirect measurements requires reliable theoretical models and accurate calibrations. On this base, Mukhamedzhanov & Pang (2018) has argued that the THM overestimates the actual $S(E)$ factor of the $^{12}\text{C}+^{12}\text{C}$ reaction. Therefore, more accurate experiments and theoretical models are needed to fix this important open issue of massive star evolution. Meanwhile, we have checked the potential impact of the THM result by computing a $20 M_\odot$ model with the Tumino et al. rate. We find that the final luminosity is only a 2% higher than that obtained with the widely adopted Caughlan & Fowler (1988) rate. An illustration of the impact of the THM rate on stellar models with lower mass, those that ignite C and Ne in degenerate conditions, can be found in Straniero et al. (2019).

⁵ <http://pdg.lbl.gov/2019/reviews/rpp2018-rev-phys-constants.pdf>

⁶ The $S(E)$ factor represents the pure nuclear contribution to the fusion cross section: $S(E) = \frac{\sigma(E)}{E \exp(2\pi\eta)}$, where E is the energy, $\sigma(E)$ the total cross section and η the Sommerfeld parameter.

Table 2. Central C mass fraction at the end of the He burning (X_c) and pre-explosive luminosity for 20 M_\odot models computed with different $^{12}\text{C}(\alpha, \gamma)^{16}\text{O}$ reaction rates. Low and high refer to the lower and upper bounds quoted by deBoer et al. (2017).

rate	X_c	$\log L/L_\odot$
Kunz et al. (2002)	0.285	5.1739
deBoer et al. (2017)	0.309	5.1739
high	0.275	5.1740
low	0.342	5.1746

The C-burning rate also scales with the square of the carbon abundance. This carbon has been previously produced during the He-burning phase. The reactions involved in the C production are: the triple- α , which represents the production channel, and the $^{12}\text{C}(\alpha, \gamma)^{16}\text{O}$, which represents the destruction channel. While the rate of the triple- α reaction is known within a 10% at the temperature of the He-burning in massive stars (Fynbo et al. 2005), the $^{12}\text{C}(\alpha, \gamma)^{16}\text{O}$ reaction rate is still rather uncertain. The rate in the STARLIB compilation is based on the Kunz et al. (2002) study. Recently, a complete reanalysis has been reported by deBoer et al. (2017). Basing on an R-matrix fit of all the available experimental data, they find a reaction rate slightly smaller than that of Kunz et al.. As a consequence a larger amount of C is expected in the center of a star at the end of the He burning phase. In Table 2, we compare the results we obtain for a set of 20 M_\odot models computed under different assumptions for the $^{12}\text{C}(\alpha, \gamma)^{16}\text{O}$ reaction rate. Within the uncertainty quoted by deBoer et al. (2017), we find a 22 % variation of the central carbon mass fraction at the end of the He-burning phase. Such a variation of the C abundance produces sizable effects on the C burning (Imbriani et al. 2001; Weaver & Woosley 1993). Indeed, a lower C abundance implies higher temperatures, smaller convective cores and, in turn, shorter C-burning lifetimes. It affects the compactness of the pre-explosive stellar structure as well as the hydrostatic and explosive nucleosynthesis. In principle, these occurrences could also affect the final luminosity. However, as noted by Straniero et al. (2016), a larger $^{12}\text{C}(\alpha, \gamma)^{16}\text{O}$ rate also implies a larger He-burning lifetime. It occurs because the $^{12}\text{C}(\alpha, \gamma)^{16}\text{O}$ reaction consumes 1/3 of He fuel compared to the triple- α , but release a similar amount of nuclear energy. As a consequence, the larger the $^{12}\text{C}(\alpha, \gamma)^{16}\text{O}$ reaction rate the slower the He consumption. In practice, this variation of the He-burning lifetime compensates the effect of the variation of the central C abundance, so that a small variation of the final He-core mass is found. As reported in the third column of Table 2, when the $^{12}\text{C}(\alpha, \gamma)^{16}\text{O}$ is varied within the uncertainty quoted by deBoer et al., such an occurrence implies negligible variations (< 0.2 %) of the final luminosity.

2.8. Chemical composition

Type II supernovae are found preferentially on the disks of spiral galaxies. Moreover, the host galaxies where the progenitors can be resolved belong to the local Universe. For these reasons, the parent stellar populations should be rather similar. Nevertheless a certain spread of the initial composition cannot be excluded. Usually a solar composition is adopted. An increase of the initial He mass fraction and/or a reduction of the initial metallicity both imply smaller envelope opacity and less efficient H-burning. The resulting stellar structures are more compact and brighter. In Figure 6 we compare the initial mass-final luminosity relations obtained by increasing the initial He mass fraction, from $Y=0.27$ to $Y=0.32$, and by decreasing the initial metallicity, from $Z=0.014$ down to $Z=0.006$, to the standard one. The masses corresponding to a pre-explosive luminosity $\log L/L_\odot = 5.1$ are reported in Table 1.

Summarizing, variations of Y and Z have opposite effects on the final luminosity. Notice that a positive correlation between the He-mass fraction and the metallicity is a natural consequence of the chemical evolution of galaxies (Pagel & Portinari 1998). For this reason a spread of the initial composition should not produce a substantial modification of our findings.

2.9. Binaries

More than 50% of massive stars are in binary (or multiple) stellar systems and most of these systems are close enough that one or more mass transfer episodes through Roche-lobe overflow may occur during the pre-supernova evolution (Sana et al. 2012). In this case, not only mass, but also angular momentum is exchanged between the components of the binary. Tidal as well as dissipative forces may also induce a synchronization of the stellar rotation rate and the orbital motion. These occurrences are expected to modify the standard paradigm of massive stars, as based on models of single star evolution. Close-binary evolution may indeed produce a variety of different evolutionary channels (Paczynski 1967; Podsiadlowski et al. 1992; Nomoto et al. 1995; Vanbeveren et al. 1998; Eldridge et al. 2008; Yoon

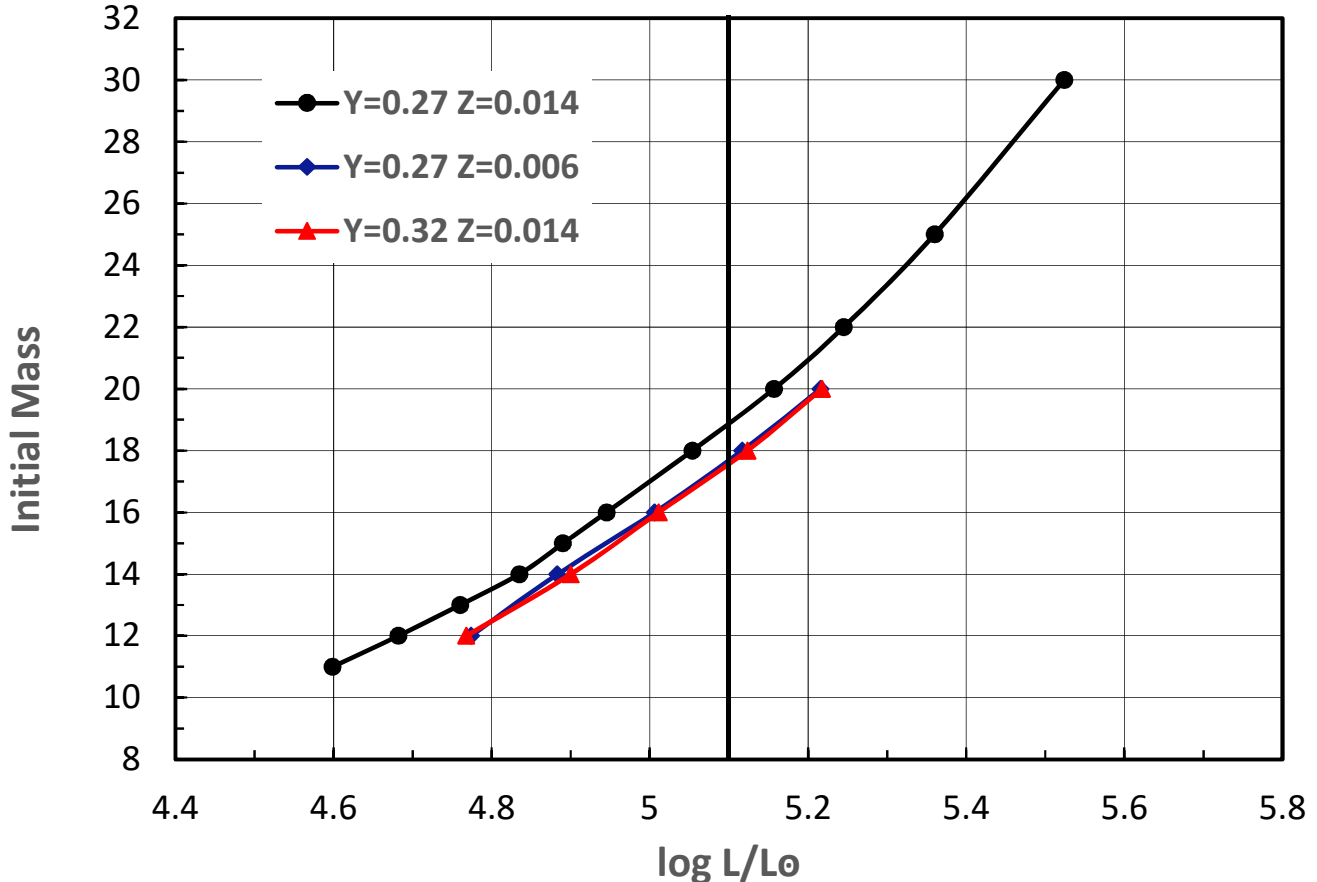


Figure 6. Initial mass-final luminosity relations for varied chemical compositions are compared to the standard (solar composition). See text for references.

et al. 2010). For this reason, the binarity is often invoked to explain peculiar objects or, more in general, to interpret the diversity of the core-collapse SN inventory. Famous examples are i) the anomalous SN1993J, whose progenitor was supposed to be a K-type supergiant hosted in a binary system with an hotter companion, and ii) the SN1987A, whose progenitor was clearly identified as a blue supergiant, possibly the secondary component of a binary with initial mass ratio close to 1 (for a review see Smartt 2009).

In general, three cases of mass transfer are usually distinguished, depending on the evolutionary status of the Roche lobe filling star. In case A, a star fills the Roche lobe during the main sequence, while in the B and C cases the mass exchange occurs when the donor is becoming or already is a red supergiant. Then, the mass lost by the donor flows through the internal Lagrangian point (L1) and eventually feeds an accretion disk around the smaller companion. It should be noted that main sequence massive stars are rather compact objects with radii of just a few R_{\odot} , so that the separation between the two components must be particularly short for a case A Roche-lobe overflow. Such kind of binaries are probably a small fraction of all the binary systems harboring massive stars. More frequent should be the other two cases, in which the Roche lobe filling star is a red or yellow supergiant.

Among the various close binary evolutionary channels, here we are interested in those that at the end of the mutual interaction leave stars with a H-rich envelope whose mass is larger than about $2-3 M_{\odot}$, so that they could be still considered as possible progenitors of type IIP SNe⁷. Let us discuss the mass donors first. In order to investigate the consequences of an enhanced mass loss due to a binary interaction on the pre-explosive luminosity, we have calculated a small set of $20 M_{\odot}$ models, in which $5 M_{\odot}$ of the H-rich envelope are artificially removed at a quite fast rate. The fast mass-loss episode is switched on at different epochs. Then, when the total mass of $15 M_{\odot}$ is attained, the mass

⁷ A lower H-mass could be enough for the rare type IIL progenitors

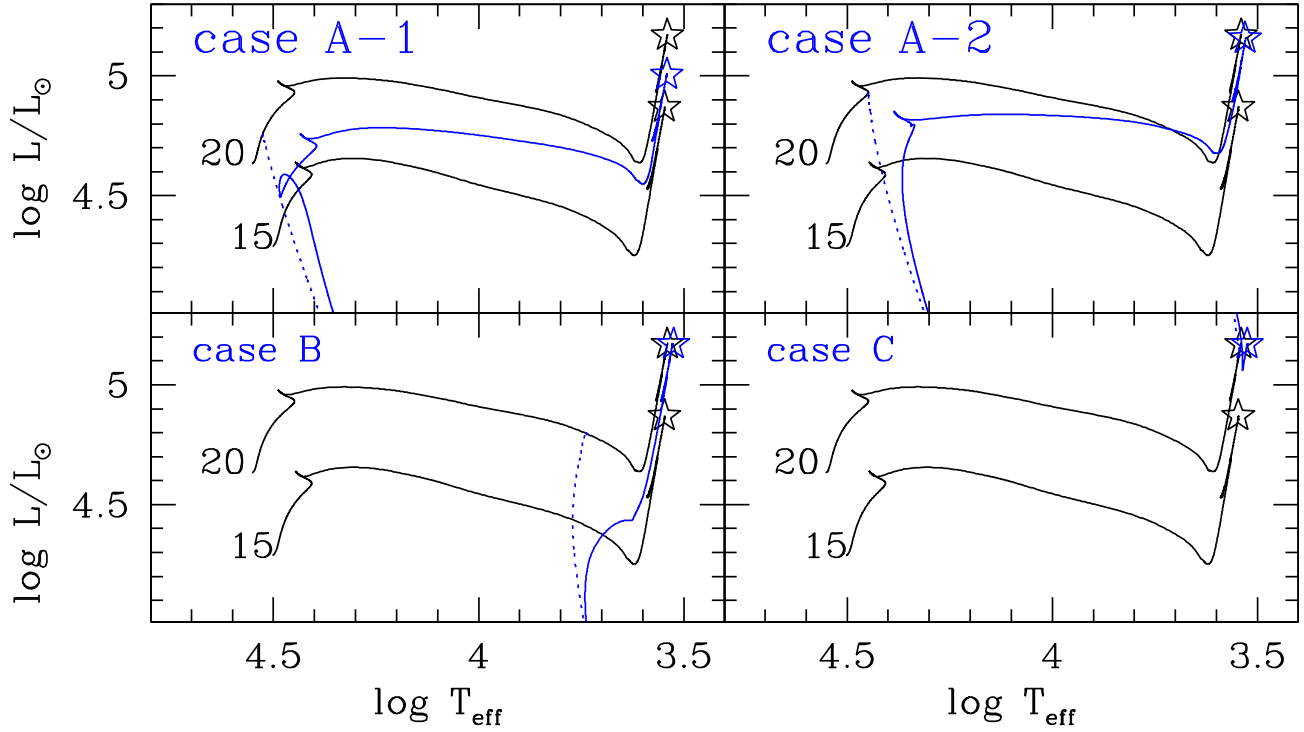


Figure 7. Effects of fast mass-loss episodes caused by Roche-lobe overflows along the evolutionary tracks of massive stars. The solid-blue lines in each panel show the evolution after a fast mass-loss episode of a star with initial mass of $20 M_{\odot}$ that loses $5 M_{\odot}$. The dotted-blue path corresponds to the mass-transfer phase. For comparison, we also report the evolutionary tracks of 15 and $20 M_{\odot}$ single star models (solid-black lines). The asterisks indicate the final models. The four cases, A-1, A-2, B and C, correspond to different choice of the epoch of the Roche-lobe overflow episode (see text for more details).

loss is switched off and the evolution has been continued up to the Si burning. No further mass transfer episodes are considered during the remaining part of the evolution. In addition we ignore the possibility of a dynamical mass transfer with the consequent common envelope episode, a phenomenon that may possibly occur in case B and C of Roche-lobe overflow, due to the presence of an extended convective envelope in the donor star. Nonetheless this simple experiment can provide a reasonable estimation of the effects of the binary interaction on the final luminosity. Four cases are here illustrated, namely: case A-1 and A-2, in which the fast mass loss takes place during the main sequence, when the central H-mass fractions are $X=0.49$ and $X=0.04$, respectively, and the corresponding radii are 7 and $12 R_{\odot}$; case B, in which the mass loss phase occurs when the star, after the main sequence, moves toward the RSG and the radius attains $281 R_{\odot}$; case C, in which the fast mass loss starts after the He-burning phase, when the radius attains $10^3 R_{\odot}$. The resulting evolutionary tracks are shown in Figure 7. Note that in case A-2, B, and C the final luminosity practically coincides with that of a single star model with $20 M_{\odot}$ (the initial mass value), while in case A-1, it is intermediate between that of the 15 and $20 M_{\odot}$ single star models. In other words, the initial mass-final luminosity relation for the donor stars is insensitive to the mass transfer, provided that it occurs close to the end or after the main sequence. In all cases, if most of the mass lost by the donor is subtracted by the accretor (conservative case), the initial mass obtained by means of the initial mass-final luminosity relation for single stars will be systematically larger than that estimated by means of the light curve fitting method. Among the 8 SNe progenitors whose mass has been derived with both methods, only one, i.e., SN2012ec, shows a similar behaviour, while the opposite is found for the others (see the discussion in section 4).

Concerning the accretors, also in this case the consequences of the mass transfer depend on the evolutionary stage at the beginning of the accretion phase. According to Podsiadlowski et al. (1992), if the accretion occurs when the star is on the main sequence, the post-accretion evolution will be very similar to that of a single star whose mass is equal to the total mass, i.e., initial mass plus the accreted mass. On the other hand, when the accretion phase starts after the exhaustion of the central H, the pre-explosive structure will be a blue or yellow supergiant (see Figure 10 in

Podsiadlowski et al. (1992)). Likely, this is a consequence of the decrease of the core mass-total mass ratio ($\xi_c = \frac{M_c}{M}$) caused by the mass accretion process. Summarizing, only main sequence accretors may produce RSG progenitors and, possibly, generate a type IIP supernova. In this case the mass estimated by means of the initial mass-final luminosity relation for single stars progenitor should coincide with that obtained with the light curve fitting method.

Finally, the possible gain of angular momentum, as due to the spin-orbit coupling, would have the same consequences illustrated in section 2.4, namely, larger core masses, brighter progenitors and, in turn, lower masses estimated by means of the initial mass-final luminosity relation.

2.10. Numerical issues

The Henyey method employed in the majority of the stellar evolution codes is a first order implicit method and the accuracy of the solutions depends on the assumed mass and time resolutions. In the FuNS code, we adopt an adaptive algorithm to select the grid of mass shells. This algorithm controls the variations between adjacent mesh points of luminosity, pressure, temperature, mass, and radius. For instance, if A is one of L, P, T, M or R , it should be:

$$0.8 \times \delta < \frac{|A(N+1) - A(N-1)|}{A(N)} < \delta, \quad (4)$$

for each shell N. In the present work we have used $\delta = 0.05$ everywhere, except for the shells located around some critical points, such as the boundaries of the convective zones, for which we use $\delta = 0.005$. This choice implies about 1000 mesh points for main sequence models and up to 5000 for the most advanced models. Recently, Farmer et al. (2016) argue that a minimum mass resolution of $0.01 M_\odot$ is necessary to achieve convergence in the He-core mass within 5%. However, as noted by Sukhbold et al. (2018), the effects of an improved resolution on the observable quantities, such as luminosity or effective temperature, are generally small. In particular, they found a weak trend to produce slightly larger He-core masses and, in turn, brighter pre-supernova models, when the zoning is finer. To check this occurrence, we have calculated a few additional evolutionary tracks with the further constraint that the difference in mass between two adjacent mesh points cannot exceed $0.01 M_\odot$. The resulting pre-explosive luminosities are less than the 1% larger than that obtained under our standard choice for the grid resolution.

3. BEYOND THE STANDARD MODEL: AXIONS

In this section we show that the emission of axions or axion like particles (ALPs) from the core of massive stars would alleviate the observed problems with the initial mass-final luminosity relation by shifting up the initial mass corresponding to the final luminosity $\log L/L_\odot = 5.1$.

The axion (Weinberg 1978; Wilczek 1978) is a light pseudoscalar particle predicted by the most widely accepted solution of the strong CP problem (Peccei & Quinn 1977) and a prominent dark matter candidate (Abbott & Sikivie 1983; Dine & Fischler 1983; Preskill et al. 1983). Its interactions with photons and fermions (f) are described by the Lagrangian terms

$$L_{\text{int}} = -\frac{1}{4}g_{a\gamma} aF_{\mu\nu}\tilde{F}^{\mu\nu} - \sum_f g_{af} a\bar{\psi}_i\gamma_5\psi_i, \quad (5)$$

where F and \tilde{F} are the electromagnetic field and its dual while the ψ_i are the fermion fields. In what follows we are interested in the coupling constants with photons, $g_{a\gamma} = C_\gamma\alpha/2\pi f_a$, and with electrons $g_{ae} = C_e m_e/f_a$, with C_γ and C_e model dependent parameters and f_a a phenomenological scale known as the Peccei-Quinn (PQ) symmetry breaking scale. The PQ scale is not fixed by the theory and is, instead, constrained by experiments and through phenomenological considerations.

Two minimal axion models are often considered as benchmarks in theoretical and experimental studies: the Kim-Shifman-Vainshtein-Zakharov (KSVZ) model (Kim 1979; Shifman et al. 1980) and the Dine-Fischler-Srednicki-Zhitnitsky (DFSZ) model (Zhitnitskii 1980; Dine et al. 1981). The most significant difference between the two models is in the couplings with electrons. The KSVZ, an example of hadronic axion, couples only to hadrons and photons at tree level. Its coupling to electrons are therefore strongly suppressed ($C_e \sim 10^{-3}$). DFSZ axions, on the other hand, couple also with electrons ($C_e \sim 1$). These QCD axion models share, however, the proportionality between the coupling constants, which measure the strength of their interactions, and the axion mass (m_a). Hence, light axions are also weakly interactive. This is reflected in Figure 8 where the diagonal yellow band, representing the region where

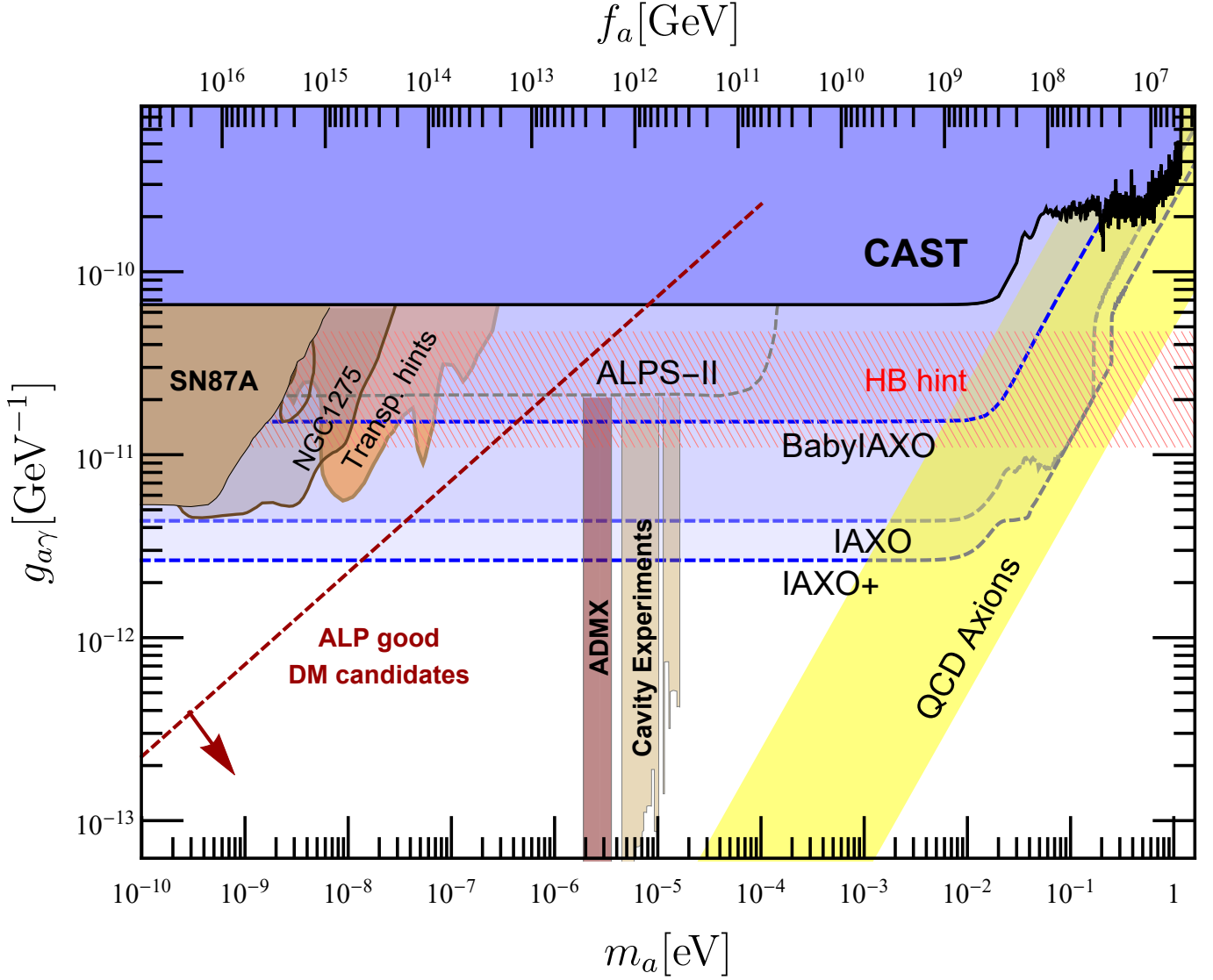


Figure 8. Overview of the axion and ALP $g_{a\gamma}$ vs. m_a parameter space, with axion hints and experiments (Di Vecchia et al. 2019). The region below the dashed red line indicates the parameters that permit ALPs to be the totality of the cold dark matter in the universe (Arias et al. 2012). Notice that the region hinted by HB stars is calculated for ALPs interacting only with photons (Ayala et al. 2014; Straniero et al. 2015). See main text for more details.

QCD axion models are expected to be found (Di Luzio et al. 2016), shows the proportionality relation between the axion mass and its coupling to photons.

More general axion-like particles (ALPs), which do not satisfy specific relations between couplings and mass, are a common prediction of string theory and other theories of physics beyond the standard model (Witten 1984; Conlon 2006; Svrcek & Witten 2006; Arvanitaki et al. 2010) though, in general, their existence is not related to the strong CP problem (Ringwald 2012). The proliferation of ALPs in extensions of the SM of particle interactions has motivated the experimental exploration of the ALP parameter space beyond the QCD axion band.

The recent years have seen an impressive experimental effort in the search of axions and ALPs (for a detailed review of the axion experimental landscape see Irastorza & Redondo 2018). Among those, helioscopes, such as the CERN Axion Solar Telescope (CAST), which search for solar axions, are the best equipped to span large ALP mass regions. The latest results from CAST (Anastassopoulos et al. 2017), shown in blue in Figure 8, have probed the axion-photon coupling down to $g_{a\gamma} = 0.66 \times 10^{-10} \text{ GeV}^{-1}$, reaching the bound from globular cluster stars (Ayala et al. 2014; Straniero et al. 2015), in the mass region $m_a \leq 0.02 \text{ eV}$. The next generation of axion helioscopes, BabyIAXO and

IAXO (Armengaud et al. 2014; Giannotti et al. 2016b; Armengaud et al. 2019) are expected to push the limit on this coupling by a factor of, respectively, ~ 3 and ~ 20 , and to further probe the QCD axion band (see Figure 8). The IAXO+ sensitivity, also shown in the Figure, represents a possible improvement of the IAXO potential with upgraded components (Armengaud et al. 2019). Axion haloscopes, such as the Axion Dark Matter eXperiment (ADMX), can reach considerable better sensitivity, though in very narrow mass bands. ADMX is already probing the QCD axion region (Du et al. 2018) and the next generation of axion haloscopes will likely explore a large portion of the QCD axion band in the mass range between $\sim 1\mu\text{eV}$ and $\sim 1\text{meV}$ (Brubaker et al. 2017; Brun et al. 2019; Alesini et al. 2017). At the same time, full laboratory experiments, such as ALPS II (Bhre et al. 2013), allow for ALP searches in part of the unexplored ALP parameter space without relying on assumptions concerning the axion source.

The axion coupling to electrons is more difficult to probe experimentally. The most stringent upper bounds have been obtained by the XENON100 collaboration (Aprile et al. 2014), $g_{ae} < 7.7 \times 10^{-12}$ (90 % CL), LUX (Akerib et al. 2017), $g_{ae} < 3.5 \times 10^{-12}$, and PandaX-II (Fu et al. 2017), $g_{ae} < 4 \times 10^{-12}$. These bounds are, however, not yet competitive with the stellar bounds on this coupling.

Besides dedicated terrestrial experiments, stellar observations offer a unique - and often very powerful - way to look at axions and other weakly interacting particles (see, e.g., Raffelt 1996, 2008). Axions with masses below a few 10 keV can be efficiently produced in stellar hot interiors through thermal processes similar to those allowing the production of neutrinos. Once produced, these weakly interactive particles can freely escape providing a net sink of energy. Considerations about stellar evolution have provided very strong bounds on the axion couplings to photons, electrons, and nucleons, often exceeding the results achieved in laboratory experiments. Currently, the strongest bounds on both the axion-photon and axion-electron coupling were derived by stellar evolution considerations. The most stringent upper bound on the axion-photon coupling, $g_{a\gamma} < 0.65 \times 10^{-10} \text{ GeV}^{-1}$ (95% CL), was obtained by Ayala et al. (2014). It is based on the measurement of the so-called R parameter, essentially the ratio of the time scales of Horizontal Branch (HB) and Red Giant Branch (RGB) stars, in 32 galactic Globular Clusters. As previously recalled, this result was recently confirmed, for ALP masses below 20 meV, by the CAST collaboration. Analogously, the most stringent experimental upper bounds on the axion-electron coupling were derived from astrophysical considerations. Miller Bertolami et al. (2014) (see also Isern et al. 2018) report $g_{ae} < 2.8 \times 10^{-13}$, as obtained from their analysis of the white dwarfs (WDs) luminosity functions, Córscico et al. (2016) find $g_{ae} < 7 \times 10^{-13}$, from the period drift of pulsating WDs, and Viaux et al. (2013b) report $g_{ae} < 4.3 \times 10^{-13}$, from the luminosity of the RGB tip of the Globular Cluster M5. These constraints can be improved using multi-band photometry of multiple globular clusters (see, e.g., Straniero et al. 2018).

More intriguingly, a series of astrophysical observations have also shown an excessive energy loss in many stellar systems, which could be accounted for by additional light, weakly interactive particles (for a recent review see Giannotti et al. 2016b). The *new-physics* interpretation of these anomalies, from observations of WDs, RGB, and HB stars, has resulted in the selection of axions and ALPs, among the various light, weakly interacting particles, as the only candidates that can explain all the excesses (Giannotti 2015; Giannotti et al. 2016a). Given the very different stellar systems in which excessive energy losses have been observed, it is quite remarkable that one single candidate can explain all the anomalies. The ALP parameter range invoked to explain the anomalous observations (at 2σ) is shown in the purple hashed region in Figure 15. The analysis indicates a preference for ALPs coupled to both electrons and photons, though a vanishing photon coupling would still be compatible with the observations within 1σ . The electron coupling, on the other hand, is predicted to be finite with a $\sim 3\sigma$ statistical significance. In any case, the hints point to a well defined area in the axion parameter space which is in part accessible to the next generation of axion probes, including BabyIAXO, IAXO and ALPS II.

3.1. Axion impact on massive stars

As discussed above, the enormous majority of results on the impact of axions on stellar evolution involves low mass stars, that is stars of mass similar or smaller than the mass of the sun. Part of the reason is that low-mass stars are the most abundant constituents of the galactic stellar populations, allowing a quite larger statistics. However, the energy loss rate via axions is very sensitive to the temperature (see the appendix) and this favors the hotter environment of the core of more massive stars. In spite of that, only a few attempts have been made to study the axion effects on the evolution of stars a few times heavier than the sun. Dominguez et al. (1999) studied the impact of axions on the Asymptotic Giant Branch (AGB) phase of low and intermediate mass stars (up to $9M_{\odot}$), showing that they produce relevant changes into the evolution and, in particular, cause a deficit of massive C-O white dwarfs. Later, Friedland

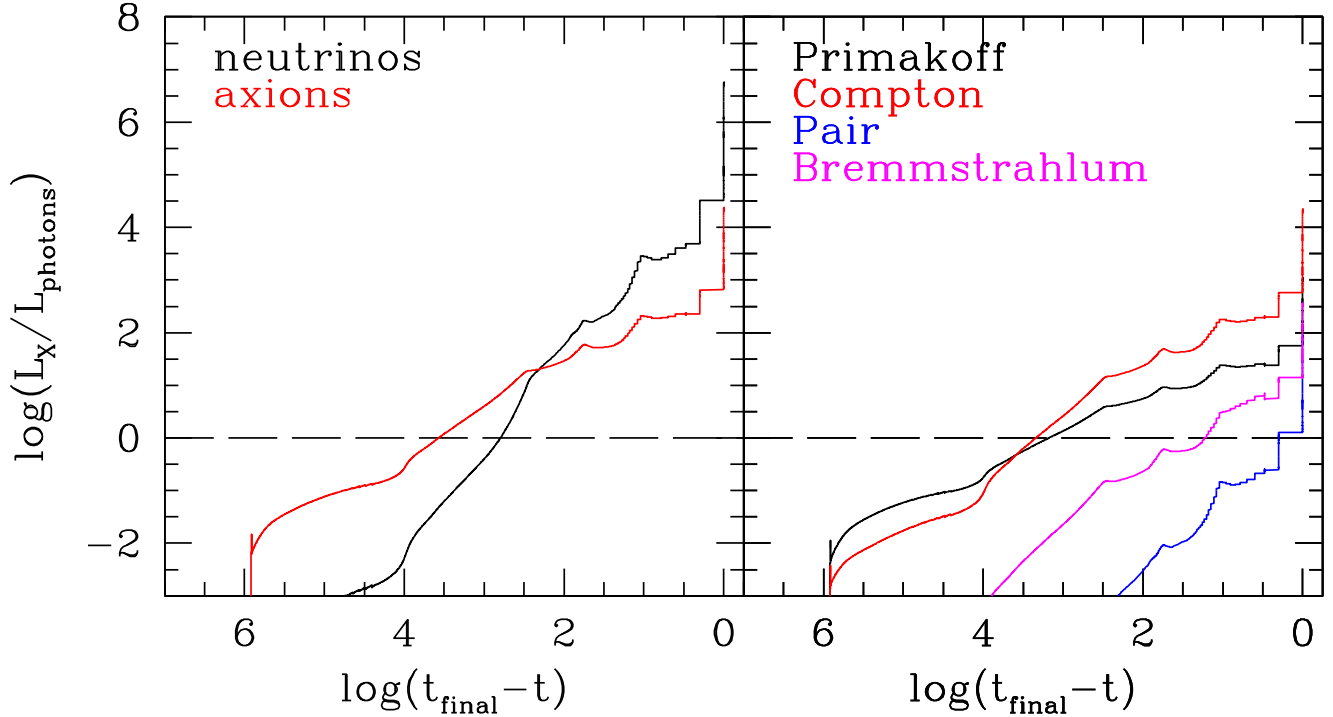


Figure 9. Left: the axion luminosity is compared to the neutrino luminosity along the evolution of a $20 M_{\odot}$ model; Right: for the same model, the Primakoff, pair, bremsstrahlung and Compton contributions to the total axion luminosity are shown. The adopted values of the axion-photon and axion-electron couplings are $g_{ae} = 4 \times 10^{-13}$ and $g_{a\gamma} = 0.6 \times 10^{-10} \text{ GeV}^{-1}$, roughly corresponding to the available experimental and astrophysical upper bounds. The evolutionary time is in yr.

et al. (2013) considered the impact of axions on the He-burning phase of solar metallicity stars with mass in the $8\text{--}12M_{\odot}$ range, focusing, in particular, on the axion effects on the blue-loops. In the present work, we are considering the impact of the axion emission on the evolution of massive stars and show how axions may reduce the pre-explosive luminosity of SN type II progenitors and, in turn, increase the estimated mass.

The axion luminosity is given by:

$$L_a = \int_0^R 4\pi r^2 \rho \epsilon_a dr \quad (6)$$

where R is the stellar radius, $\rho(r)$ and $T(r)$ the density and the temperature internal profiles, and $\epsilon_a(\rho, T)$ is the rate of energy drained by axions per unit mass (see appendix). In the hot plasma of a star, ϵ_a takes contribution mostly from the following processes:

1. Primakoff, i.e., photon-axion conversion in the electrostatic field of electrons and ions;
2. Compton, i.e., scattering of photons on electrons or ions;
3. electron-positron annihilation $e^+e^- \rightarrow \gamma + a$, also known as pair production;
4. bremsstrahlung $e + Ze \rightarrow e + Ze + a$ on electrons and nucleons.

The numerical recipes we have used to estimate these rates are summarized in the appendix, so the results can be reproduced and tested in future analyses.

The expected axion luminosity along the whole evolution of a $20 M_{\odot}$ star is shown in Figure 9. In the right panel, we show the contributions to the total axion luminosity due to the four production processes described above. It is evident that the Primakoff and the Compton contributions are the major sources of axions in these massive stars. In the left panel, we compare the total axion luminosity to the thermal neutrino luminosity. Axions clearly represent a significant energy sink in these stars, which is much larger than that induced by neutrinos for a considerable portion

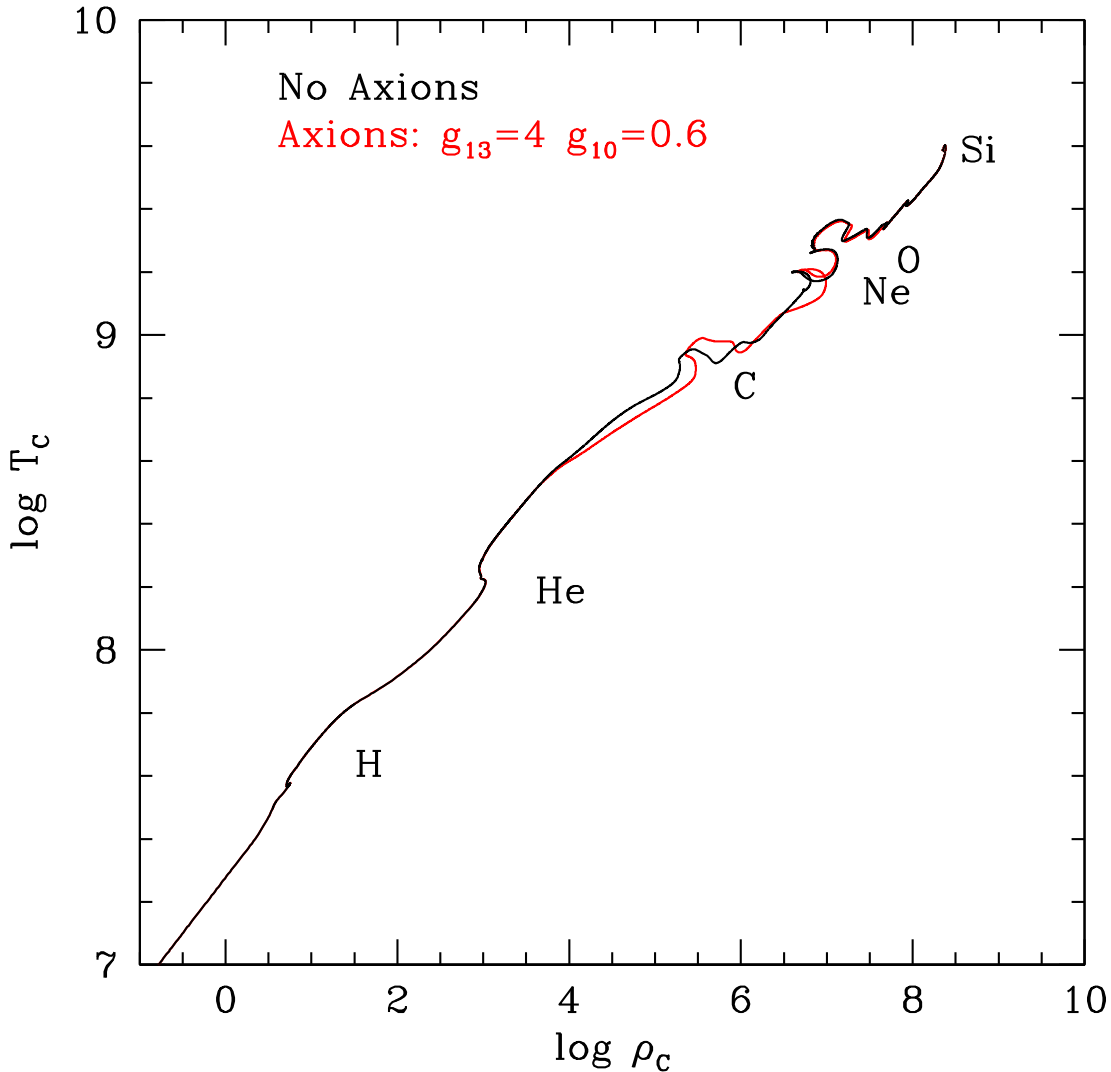


Figure 10. Central temperature versus central density for two $20 M_{\odot}$ models: standard (no axions), black line, and non standard ($g_{10} = g_{a\gamma}/10^{-10} \text{ GeV}^{-1} = 0.6$ and $g_{13} = g_{ae}/10^{-13} = 4$), red line.

of the evolution. In particular, major effects are produced starting from the late part of the He-burning phase. As shown in Figure 10, when the axion energy loss is considered, the C burning and the Ne burning take place at higher temperature and density. Moreover, the envelope freeze-out occurs earlier than in standard models. Consequently, the final luminosity is substantially lower (see Figure 11). In addition, axions may also affect the compactness of pre-explosive models. We recall that the evolutionary tracks presented in this paper have been stopped when the maximum temperature attains ~ 4 GK. The final mass distribution within the core of the two $20 M_{\odot}$ evolutionary tracks, with and without axion energy loss, are compared in Figure 12. As expected, the axion model shows a higher mass concentration in the $0.006\text{-}0.03 R_{\odot}$ region. However, the innermost portion of the core ($M < 1.6 M_{\odot}$) is not affected by axion.

Then, we have computed two additional set of stellar models. In the first one we have included the energy loss induced by the axion-photon coupling alone, namely $g_{a\gamma} = 0.6 \times 10^{-10} \text{ GeV}^{-1}$ and $g_{ae} = 0$. In this case, only the Primakoff process is activated. This choice would be appropriate for, e.g., a pure *hadronic* axion model, such as the KSVZ, or an ALP coupled with photons only, with a coupling close to the astrophysical and experimental upper bound. In the second set of stellar models we have switched on the contribution from the axion-electron coupling by fixing $g_{a\gamma} = 0.6 \times 10^{-10} \text{ GeV}^{-1}$ and $g_{ae} = 4 \times 10^{-13}$, corresponding roughly to the limit from globular cluster stars. The initial mass-final luminosity relations for non-rotating and rotating massive star models are reported in Figure 13.

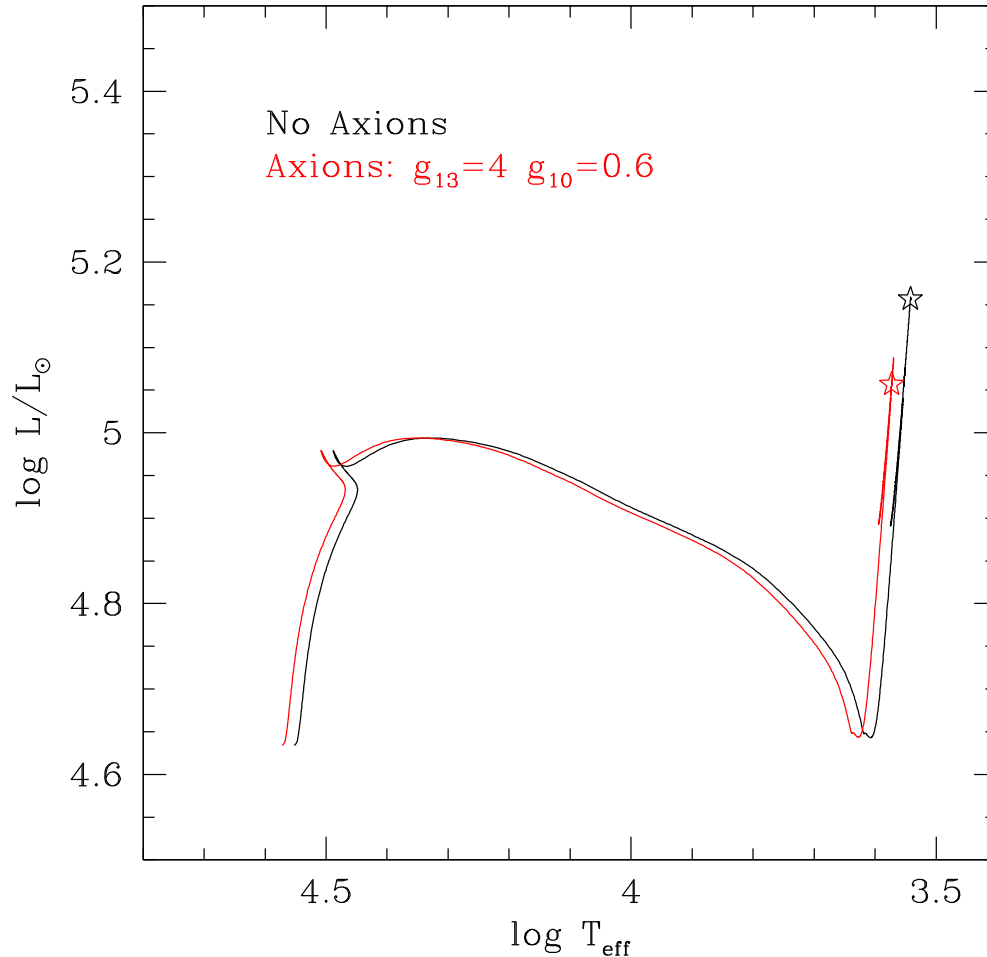


Figure 11. The evolutionary tracks of the two models of Figure 10. An offset of $\Delta \log T_{eff} = 0.02$ has been applied to the non-standard track. The final T_{eff}, L points are marked with a black and a red star, respectively. Note that the model with axions attains a maximum luminosity at the beginning of the C burning. Then, during the C burning, the track moves to a slightly fainter point, where remains until the final collapse.

The initial masses corresponding to a final luminosity $\log L/L_{\odot} = 5.1$ are 19.7 and 20.9 for the models with the axion-photon coupling only and the models with both the axion-photon and the axion-electron couplings, respectively.

Worth of notice is the peculiar low final luminosity we found in the case of the $14 M_{\odot}$ model, namely $\log L/L_{\odot} = 4.37$, of the second set of axion models. The plot of the corresponding evolutionary track illustrates the origin of this result (see Figure 14). Indeed this model experiences an extended blue loop during the He burning phase, but at variance with the standard evolutionary track (no axions), the model with both the axion-photon and axion-electron couplings does not complete this loop returning on the red supergiant branch at the end of the He burning. Instead the luminosity freeze-out occurs before the star closes its blue loop, so that the final point is substantially fainter and bluer than that obtained in the standard case. We found that this behaviour affects the evolutionary tracks of models with mass in a restricted range around the $14 M_{\odot}$, while the $13 M_{\odot}$ model, that also experiences a blue loop, shows a normal behaviour.

3.2. A new hint of axions? Experimental considerations

We have shown that axions would substantially modify the initial mass-final luminosity relation of massive stars, thus moving to higher values the mass range of type II SN progenitors. Axion also represent an appealing solution for various stellar anomalies, such as those related to the white dwarf cooling rate. The considerable larger amount of white dwarfs and type II progenitors expected from the LSST deep photometric survey will definitely shed light on these problems (Drlica-Wagner et al. 2019; Bechtol et al. 2019). Moreover, the axion experimental proposals of the

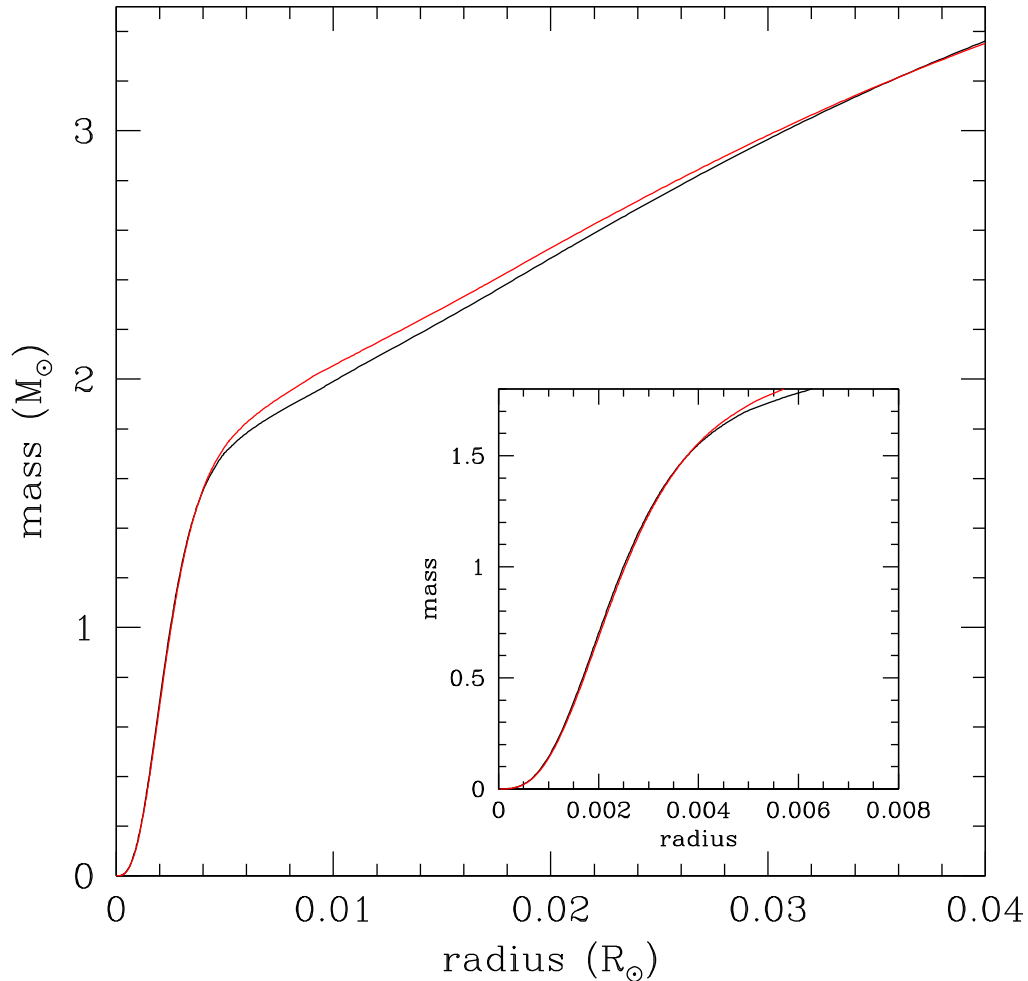


Figure 12. Effects of the axion energy loss on the mass distribution within the core of the last computed models of the two evolutionary tracks shown in Figure 11. The innermost portion of the core is enlarged in the inset.

next generation could possibly test this hypothesis. In order to make our results more clear from an experimental point of view and to guide the experimental effort, here we make some general considerations and study the potential of proposed axion experiments.

As seen, the emission of axions shifts up the initial mass that corresponds to $\log L/L_\odot = 5.1$, where L is the final stellar luminosity. The exact shift depends on several physical parameters. However, we have found a reasonable parametrization as the sum of terms proportional to the square of the coupling constants:⁸

$$\frac{\Delta M}{M_\odot} \approx 2.2 \left(\frac{g_{a\gamma}}{10^{-10}} \right)^2 + \frac{1.5}{16} \left(\frac{g_{ae}}{10^{-13}} \right)^2 \quad (7)$$

The parameter band corresponding to the mass shift $0.5M_\odot \leq \Delta M \leq 3M_\odot$, as derived from the above equation, is shown as a gray hushed area in Figure 15. The Figure shows also the experimental potential to explore the region with proposed experiments including BabyIAXO and IAXO [citation], ALPS II (Bhre et al. 2013) and DARWIN (Aalbers et al. 2016). In the case of CAST, BabyIAXO, IAXO and ALPS II, the experimental potential assumes low mass ALPS. The region hushed in purple in the Figure is the one inferred from observations of low mass stars (Giannotti et al. 2016b). The area overlaps, albeit in a small region, with the parameters required for a mass shift $\Delta M \lesssim 1M_\odot$.

⁸ The relation is only an approximate fit. A more accurate relation would require the coefficients to depend on ΔM . However, the result is fairly accurate for $\Delta M \approx 0.5 - 3M_\odot$.

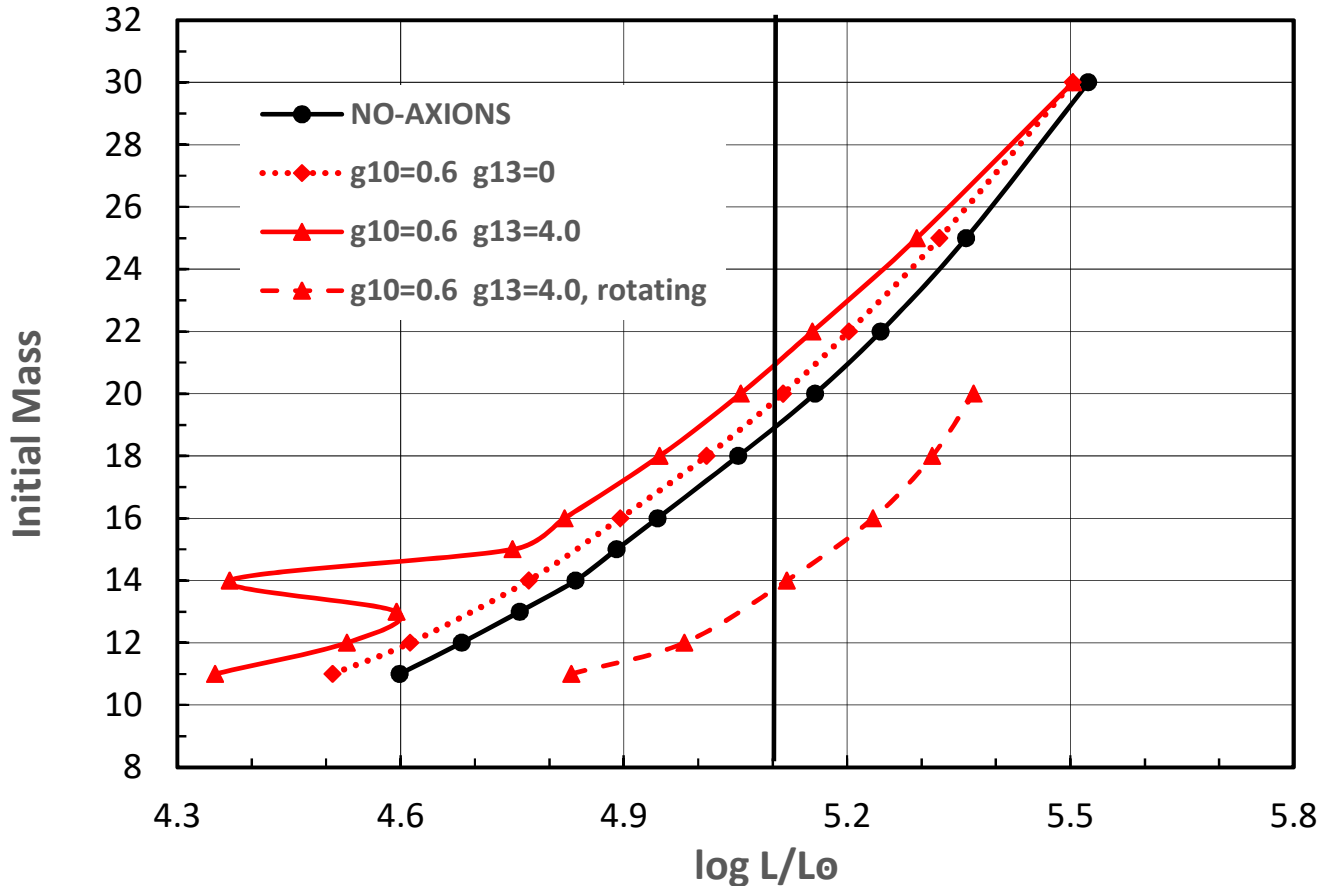


Figure 13. Rotating and non-rotating initial mass-final luminosity relations for models with axion energy sink (red lines) are compared to that from non-rotating standard models (black line). The red-dashed line, relative to rotating models, has been obtained with the same set of rotation parameters of the dashed line in Figure 5.

Larger mass shifts require a larger electron coupling (larger photon couplings are already excluded by CAST, at least at mass below ~ 20 meV). In any case, the parameter range is accessible to the next generation of axion helioscope experiments as well as to ALPS II. On the other hand, as evident from the Figure, WIMP detectors such as LUX, or even the future DARWIN detector, do not have the capability to probe ALP parameters that give a mass shift up to a few M_{\odot} .

QCD axions deserve a separate analysis. Because of the mass-coupling relation, the axion couplings of interest for stellar evolution imply masses of ~ 10 - 100 meV, and could not be detected by the helioscope experiments, except for IAXO. Figure 16 shows the parameter space for the DFSZ axion, which may interact with both electrons and photons, together with the regions excluded by stellar evolution considerations. The main result is that an upward shift of about $2M_{\odot}$ of the initial masses of SN IIP progenitor is allowed when the RGB and HB bounds to the axion couplings are assumed. Moreover, IAXO would definitely be able to test the possibility that DFSZ axions are indeed responsible for the missing energy required in our problem.

4. SUMMARY AND CONCLUSIONS

In this paper we have revised the initial mass-final luminosity relation obtained from state-of-the-art massive star models. Standard and non-standard physical processes which determine this relation are discussed in some details. We find, in particular, that different combinations of initial parameters, such as the mass and the rotational velocity, lead to similar final-He-core masses and, in turn, to similar pre-explosive luminosities. Moreover, the final luminosity also depends on the initial composition. In other words, the final luminosity is not a function of only one variable, i.e., the initial mass. This degeneracy of the initial parameters is often ignored when the pre-explosive luminosity is used to estimate the progenitor mass. In the rest of this section we will analyze this issue.

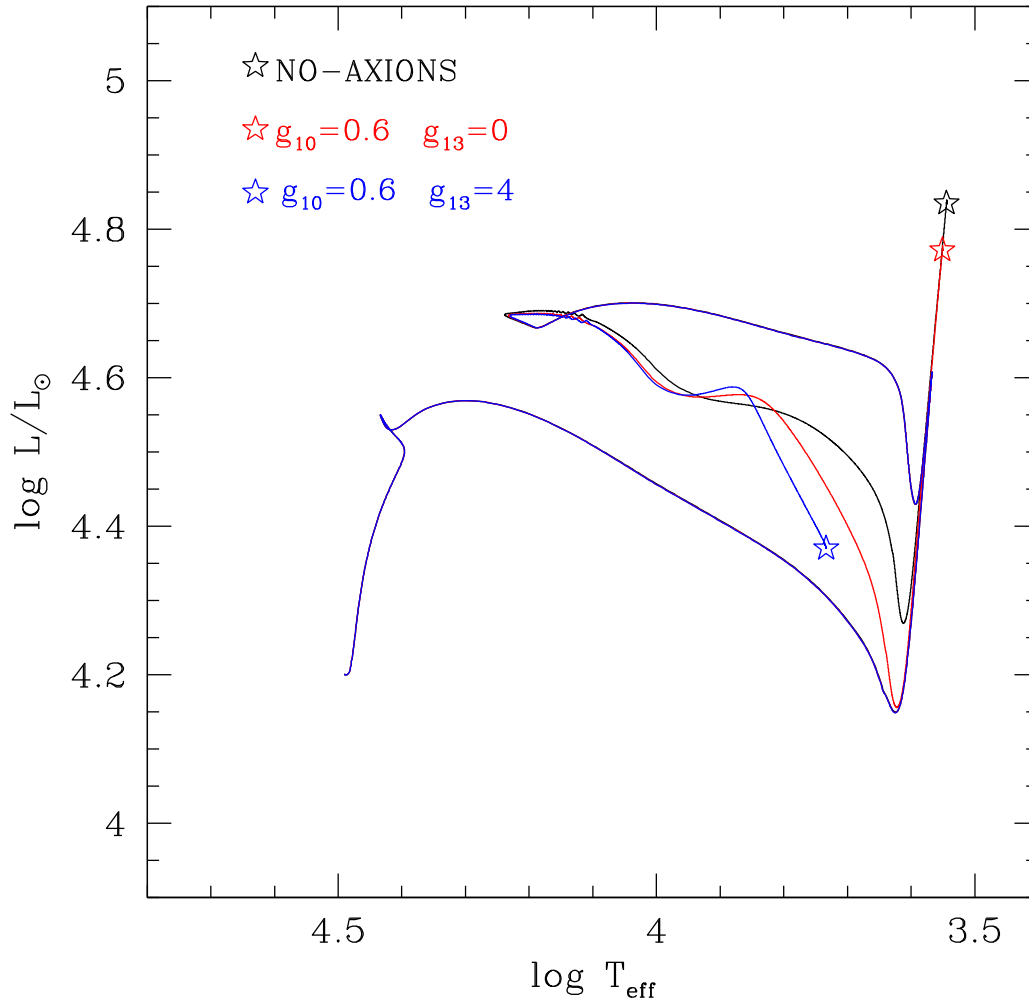


Figure 14. Evolutionary tracks of the $14 M_{\odot}$ models with and without axions.

In the HR diagram reported in Figure 17, the pre-explosive $\log T_e$, $\log L$ positions of type II supernovae progenitors (Smartt 2015; Davies & Beasor 2018) are superimposed to some of our standard (non-rotating) evolutionary tracks. The two open square refers to type IIL supernovae, while the filled circle represent type IIP supernovae. Notice that after the revision of the bolometric corrections discussed in Davies & Beasor (2018), the upper bound of the pre-explosive luminosity is now slightly larger than that previously found by Smartt (2015). According to Davies & Beasor (2018), three progenitors show pre-explosive luminosity $\log L/L_{\odot} \sim 5.2$. Worth to notice, two of these three points correspond to the only two type IIL progenitors, SN2009kr and SN2009hd, while the third, SN2012ec, we suspect it was a fast rotating main-sequence stars (see below). The initial masses estimated by means of the FuNS evolutionary tracks ($v_{ini} = 0$) are in the range $9 < M/M_{\odot} < 20$, but excluding the three brightest objects, the upper bound is just $\sim 17 M_{\odot}$.

As mentioned in the introduction an independent estimation of the progenitor mass can be obtained from the best fit of the observed properties of SN light curves (LCs). Only 8 SNe IIP are in common between the Morozova et al. (2018) and the Smartt (2015) samples. Pre-explosive luminosities and initial masses of the corresponding progenitors are listed in Table 3. Although independent on the final luminosity, the LC best fit method also relays on theoretical models. Morozova et al. (2018) have used, in particular, KEPLER progenitors to model the outgoing shock and its interaction with the dense circumstellar material surrounding the exploding progenitor. Therefore, in Figure 18 we compare their results with the masses derived from the pre-explosive luminosity and the initial mass-final luminosity relation from (non-rotating) KEPLER models. Nonetheless, negligible differences of this Figure would have been found if we had used our initial mass-final luminosity relation.

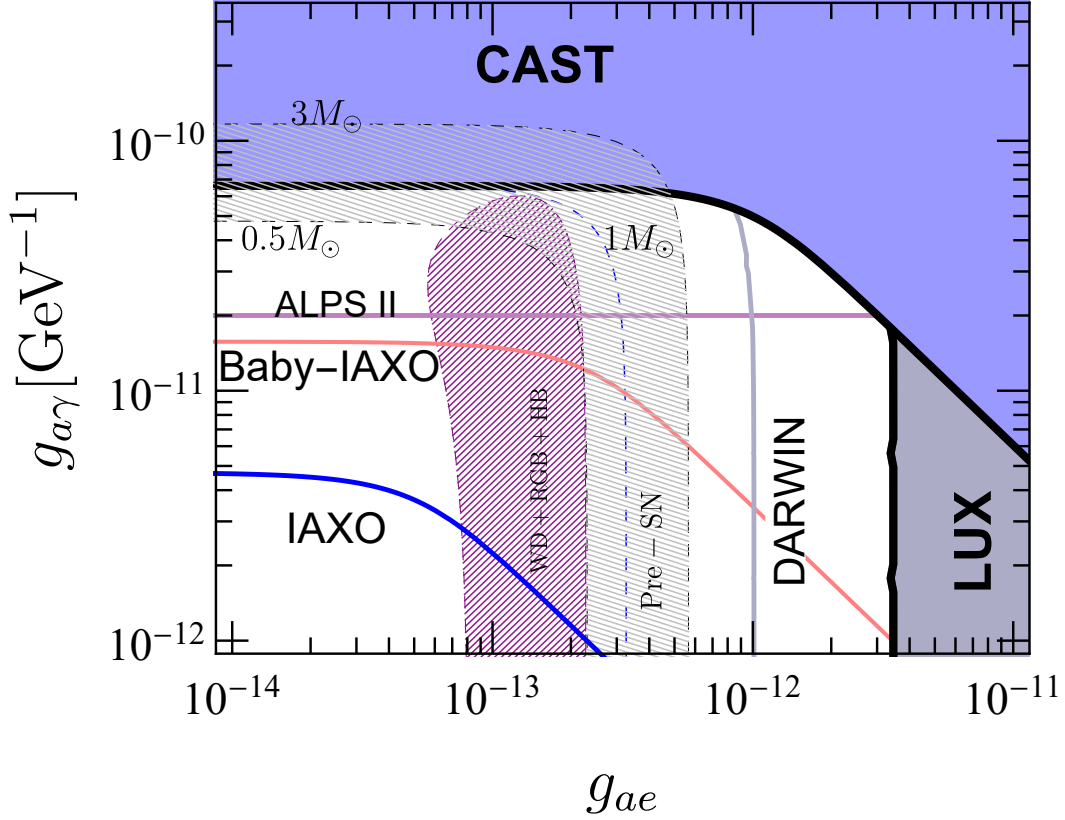


Figure 15. Mass shift for generic ALPs in comparison with the current and planned experimental potential. The parameter regions covered in color are already excluded by current experiments. The expected experimental potential of the next generation of axion experiments is indicated with continuous lines. The hushed purple region indicates the $2\text{-}\sigma$ axion hints from low mass stars (Giannotti et al. 2016b; Di Vecchia et al. 2019) while the gray hushed region covers the axion parameters that would give ΔM between 0.5 and $3M_{\odot}$. The line corresponding to $\Delta M = 1M_{\odot}$ is also indicated, for reference.

Table 3. Data for SN IIP progenitors. Column 2: pre-explosive $\log L/L_{\odot}$ from Davies & Beasor (2018), with the corresponding 1σ error; column 3: most probable mass (in M_{\odot}) from (Morozova et al. 2018) with the corresponding 95% C.L. mass range.

Supernova	$\log L$	M
SN2004et	4.77 ± 0.07	$16.5_{15.0}^{22.0}$
SN2005cs	4.38 ± 0.07	$9.5_{9.0}^{12.0}$
SN2012A	4.57 ± 0.09	$9.5_{9.0}^{14.0}$
SN2012aw	4.92 ± 0.12	$20.0_{19.0}^{22.5}$
SN2013ej	4.69 ± 0.07	$10.5_{9.0}^{18.0}$
SN2012ec	5.16 ± 0.07	$13.0_{10.0}^{18.5}$
SN1999em	< 5.02	$21.5_{16.5}^{22.0}$
SN1999gi	< 4.85	$12.0_{9.0}^{17.0}$

Six out of eight data points clearly stay above the median, while just one, SN2012ec, is definitely below it. Excluding SN2012ec, it results that the masses from the LC best fit are $2.91 \pm 0.84 M_{\odot}$ higher, on the average, than those estimated from the pre-explosive luminosity. This discrepancy worsens when convective-core overshoot or rotation are taken into account (see section 2). Indeed, both these processes imply larger He-core masses and, in turn, brighter progenitors, so that the masses derived from the corresponding initial mass-final luminosity relation are smaller. Other missing

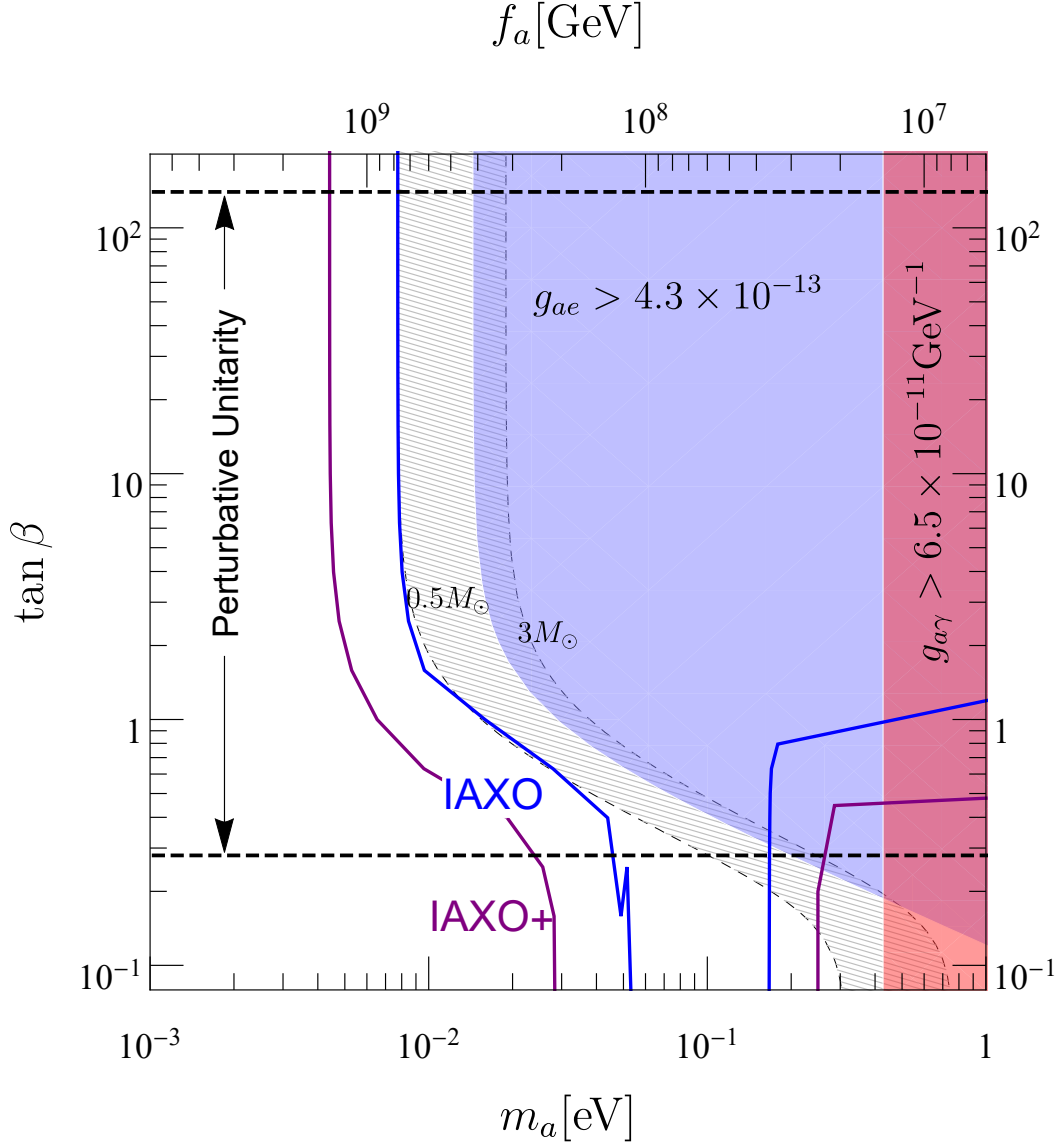


Figure 16. Axion parameter space for the DFSZ axion model, with the expected IAXO experimental potential (Armengaud et al. 2019) and the regions excluded by other astrophysical considerations: $g_{a\gamma} > 6.5 \times 10^{-11} \text{ GeV}^{-1}$ (light red region), from the R-parameter (Ayala et al. 2014), and $g_{ae} > 4.3 \times 10^{-13}$ (light blue region), from the luminosity of tip of the RGB stars in M5 (Viaux et al. 2013b). The set of axion parameters that give a progenitor mass shift between $0.5M_{\odot}$ and $3M_{\odot}$ is enclosed in the gray hushed region. The RGB bound corresponds to $\Delta M \approx 2M_{\odot}$. The regions of $\tan\beta$ below 0.28 and above 140 are excluded by the requirement that the Yukawa couplings to fermions satisfy perturbative unitarity. The bound from CAST, BabyIAXO and ALPS II do not apply in this case.

physical processes, like enhanced mass loss due to a binary mass transfer episode (section 2.9) or envelope heating driven by internal gravity waves (section 2.5), would also worsen the tension.

If the effect of convective-core overshoot may be negligible, rotation is a quite common feature of massive stars. According to Hunter et al. (2008, 2009), the projected rotational velocity ($v \sin i$) of massive H-burning stars ranges between 0 and 300 km s^{-1} and, when the mass range is limited to stars with $M < 25 M_{\odot}$, the distribution peaks between 100 and 150 km s^{-1} . This evidence reinforces our claim of a discrepancy between the masses estimated by means of the SN light curve and those derived from pre-explosive luminosities. Indeed, when rotational velocities of this order of magnitude are considered, the masses estimated from the final luminosity are up to $6 M_{\odot}$ smaller (see section 2.4 and Table 1). Fast rotation may be eventually invoked to explain SN points located below the median in Figure 18. For instance, even the extreme case of SN2012ec can be fitted by assuming a large initial rotational velocity

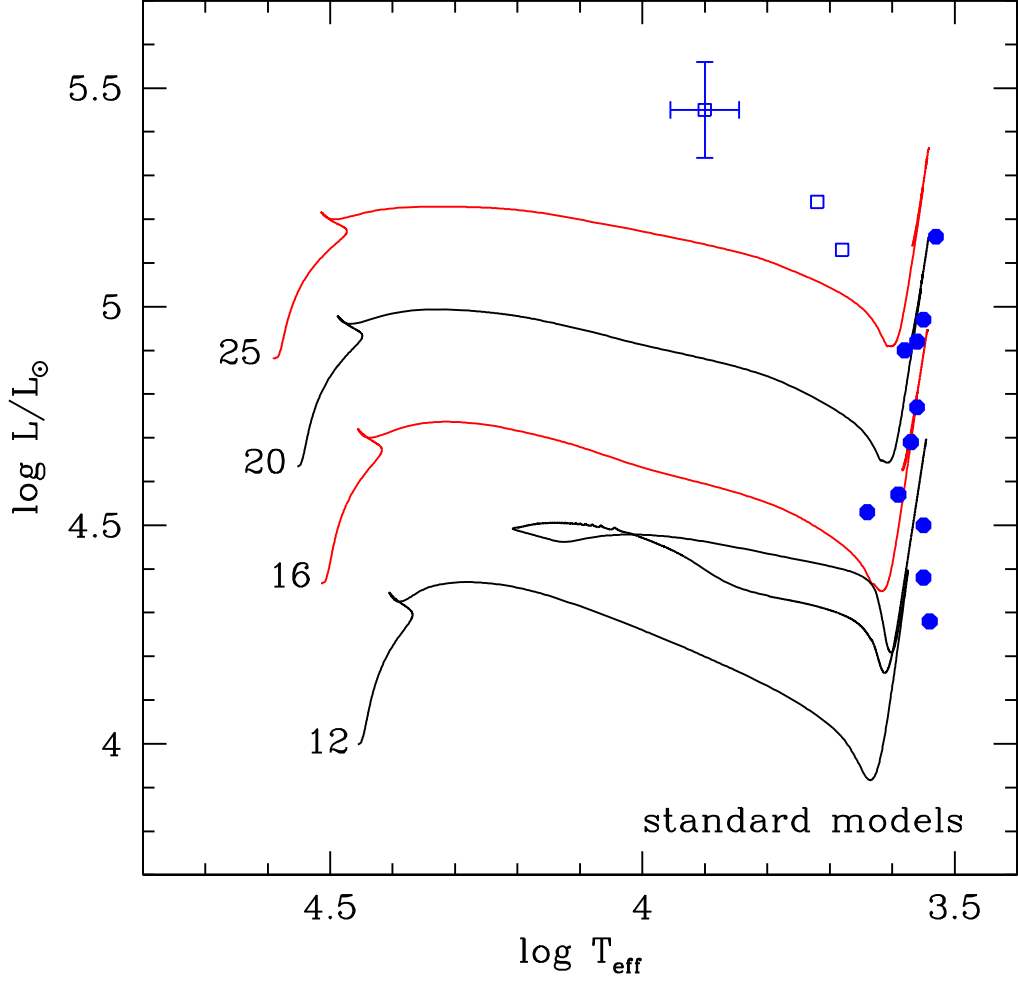


Figure 17. Standard evolutionary tracks (no rotation, no axions). The data-points represent SN IIP progenitors (filled circles) and SN IIL progenitors (open squares), from [Davies & Beasor \(2018\)](#). The average error bar is shown.

Table 4. Masses (in M_{\odot}) estimated from the observed pre-explosive luminosities listed in Table 3, as obtained by means of different initial mass-final luminosity relations, namely: non-rotating KEPLER models, non-rotating FuNS models with axion energy loss, rotating ($v_{ini} = 200 \text{ km s}^{-1}$) FuNS models with axion energy loss. The axion parameters are $g_{10} = 0.6$ and $g_{13} = 4$. Blank spaces correspond to unrealistic extrapolations of the initial mass-final luminosity relations, i.e., values below $9 M_{\odot}$.

	KEPLER $v_{ini} = 0$	FuNS+AX $v_{ini} = 0$	FuNS+AX $v_{ini} = 200$
SN2004et	$12.2^{+1.2}_{-1.1}$	$15.3^{+1.0}_{-1.0}$	
SN2005cs		$11.0^{+0.5}_{-0.6}$	
SN2012A	$9.2^{+1.3}_{-1.2}$	$12.8^{+1.0}_{-1.0}$	
SN2012aw	$14.9^{+2.3}_{-2.1}$	$17.6^{+2.1}_{-1.9}$	$11.4^{+1.4}_{-0.9}$
SN2013ej	$10.9^{+1.1}_{-1.1}$	$14.2^{+0.9}_{-0.9}$	
SN2012ec	$19.7^{+1.5}_{-1.5}$	$22.0^{+1.4}_{-1.5}$	$14.8^{+1.4}_{-1.2}$
SN1999em	< 16.8	< 19.3	< 12.5
SN1999gi	< 13.6	< 16.4	< 10.8

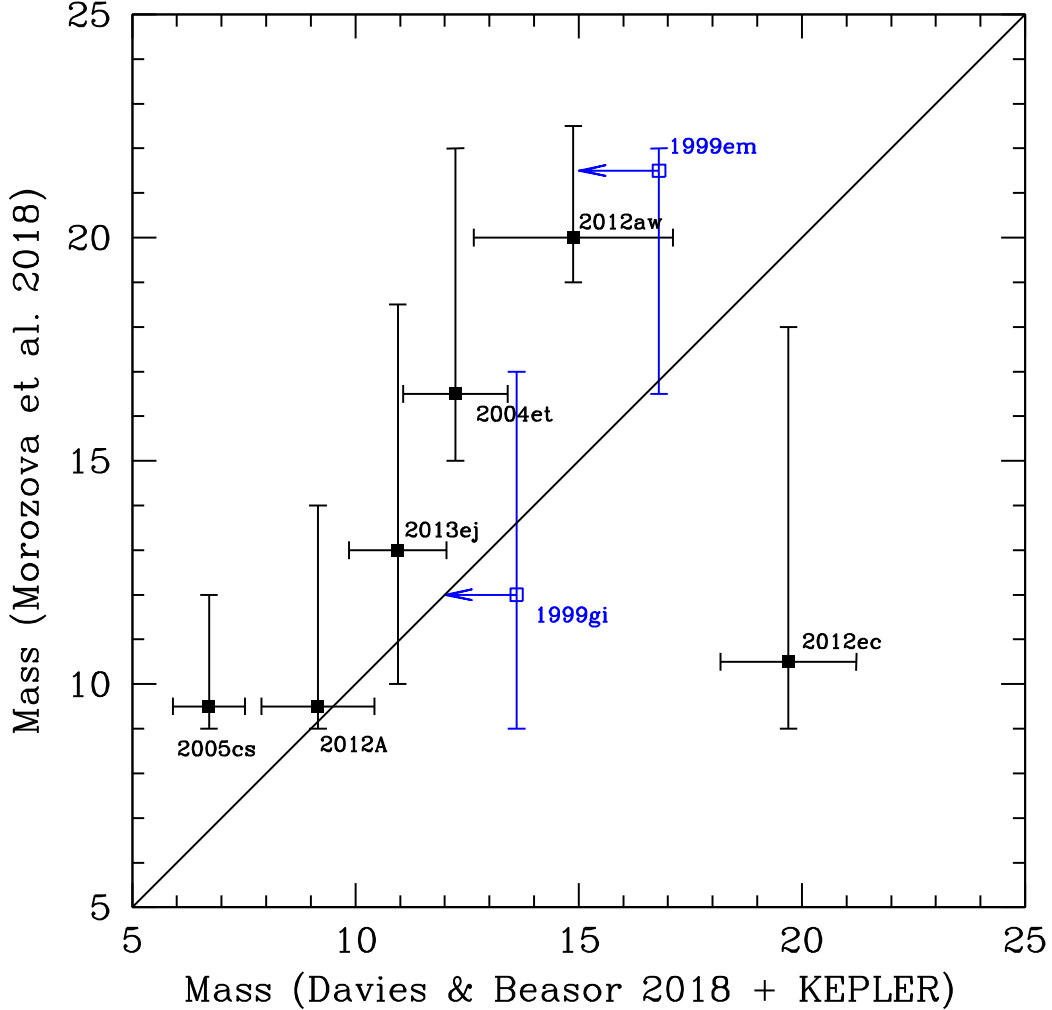


Figure 18. Masses of SN IIP progenitors obtained by [Morozova et al. \(2018\)](#) basing on the analysis of the explosive outcomes versus those derived from the observed pre-explosive luminosities ([Davies & Beasor 2018](#)) and the KEPLER initial mass-final luminosity relation.

($\sim 200 - 300 \text{ km s}^{-1}$). Indeed, the mass inferred from the LC best fit is significantly smaller than that derived from the pre-explosive luminosity of non-rotating models ([Barbarino et al. 2015](#); [Morozova et al. 2018](#)). This occurrence is also confirmed by the mass estimate independently obtained from the O yield of the SN2012ec ([Valenti et al. 2016](#); [Davies & Beasor 2018](#)). A spread of initial rotational velocities also provide a natural explanation of the lack of a direct correlation between initial mass and final luminosity.

In any case, the initial mass-final luminosity relation from non-rotating models should represent the upper bound to the initial masses. In contrast, some progenitors, such as SN1999em, SN2004et and SN2012aw, show much higher masses than expected. For example, in the case of SN2004et, the maximum mass inferred from the pre-explosive luminosity is $12.2 \pm 1.1 M_{\odot}$, while Morozova et al. found a most probable mass of $16.5 M_{\odot}$, with a 95% C.L range between 15 and $22 M_{\odot}$. Notice that a previous estimate of the mass range for this supernova progenitor based on LC best fit was $24-29 M_{\odot}$ ([Utrobin & Chugai 2009](#)). Similarly, for SN2012aw Morozova et al. found a most probable value of $20 M_{\odot}$ ($19-22 M_{\odot}$ is the 95% C.L. range, see also [Barbarino et al. \(2015\)](#)), while the maximum mass compatible with the observed pre-explosive luminosity, as obtained from non-rotating (no-overshoot) models, is just $14.9 \pm 2.3 M_{\odot}$ (see Table 4).

In spite of the limited sample of supernovae, our analysis suggests that behind this problem there is a clue of missing physical processes. The most natural way to reduce the final luminosity and, in turn, allow more massive progenitors, is to increase the rate of energy loss. As seen in the previous section, the inclusion of axion production in the calculations

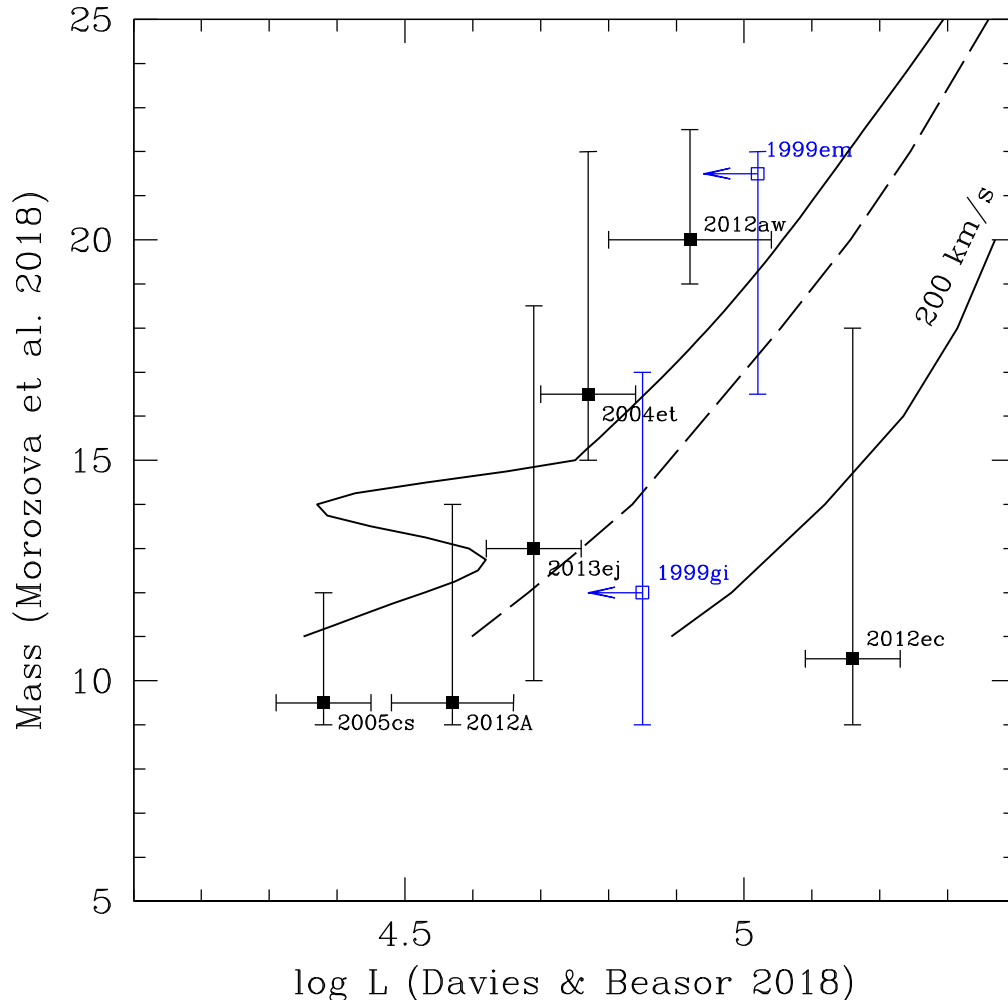


Figure 19. Theoretical versus observed initial mass-final luminosity relation. The observed mass and luminosity are those listed in Table 3. The theoretical relations (black-solid lines) are derived from FuNS models with axion energy loss ($g_{10} = 0.6$, $g_{13} = 4$) and with or without rotation. For comparison, the FuNS standard relation is also shown (dashed line).

of massive star models would imply a sizable increase of the progenitor masses estimated by means of the observed pre-explosive luminosity. In particular, depending on the assumed couplings of axions with other standard particles (cfr. Figure 15 and 16), the resulting progenitor masses are up to $\sim 3M_{\odot}$ larger than those obtained without axions. As an example, in Table 4 we report the masses of the 8 SNe progenitors already listed in Table 3 as obtained by means of the initial mass-final luminosity relations derived from models with axion, by assuming $g_{a\gamma} = 0.6 \times 10^{-10} \text{ GeV}^{-1}$ and $g_{ae} = 4 \times 10^{-13}$, for the axion-photon and the axion-electron couplings, respectively. The axion scenario is illustrated in Figure 19, where we show the initial masses from the LC best fit (Morozova et al. 2018) versus the observed pre-explosive luminosity (Davies & Beasor 2018), but superimposed are the theoretical relations we obtained including axions and initial rotational velocity $v_{ini} = 0$ and 200 km s^{-1} . For comparison, we also show the standard relation (no-axion) for non-rotating models.

Summarizing, we have shown that the initial mass-final luminosity relation is a powerful tool to investigate physics beyond the Standard Model. In spite of the limited data sample, the available measurements appear incompatible with the standard picture and suggest possible hints in favor of an enhanced energy loss rate from weakly interactive particles. In particular, once a spread of initial rotational velocity is assumed in agreement with the extant measurements of this quantity, the best reproduction of the available sample of initial mass-final luminosity data is obtained with models that account for the production of axions or ALPs. The choice of axions/ALPs as the new physics candidates proposed to solve this problem is dictated by the current interest in axion research and the confidence that our hypothesis may

be tested in the near future. However, we cannot exclude that other new physics processes are at work. For instance a similar effect could be caused by the thermal production and emission of dark photons. On the base of the present analysis, such a possibility is not excluded.

O.S and L.P. are supported by the Italian Space Agency (ASI) and the Italian National Institute of Astrophysics (INAF) under the agreement n. 2017-14-H.0 - *attività di studio per la comunità scientifica di Astrofisica delle Alte Energie e Fisica Astroparticellare*. I.D. is supported by the MICINN-FEDER project AYA2015-63588-P and A.M. by the Istituto Nazionale di Fisica Nucleare (INFN) through the “Theoretical Astroparticle Physics” project and by Ministero dell’Istruzione, Università e Ricerca (MIUR).

APPENDIX

A. AXION EMISSION RATES

In this appendix we provide the numerical recipes used to calculate the axion emission rates. The density of the j ions is

$$n_j = \frac{\rho}{m_u} \frac{X_j}{A_j}, \quad (\text{A1})$$

where $m_u = 1.66 \times 10^{-24}$ g is the atomic mass unit and X_j , A_j , and Z_j are the mass fraction, the atomic mass, and the charge of the j specie, respectively. Then, the electron density is

$$n_e = \frac{\rho}{m_u \mu_e}, \quad (\text{A2})$$

with the mean electron molecular weight defined by

$$\frac{1}{\mu_e} = \sum \frac{X_j Z_j}{A_j}, \quad (\text{A3})$$

In the following, the temperature, T , and the mass density, ρ , are in K and g cm^{-3} , respectively. We indicate with ε the energy loss rates in $\text{erg g}^{-1} \text{s}^{-1}$.

A.1. Primakoff production

The Primakoff production of axions in a stellar core, that is the production of axions from thermal photons conversion in the electrostatic field of the nuclei or of the electrons $\gamma + Ze \rightarrow \gamma + a$, is widely discussed in the literature (e.g., Raffelt (1986); Raffelt & Dearborn (1987)). Our method is based on Raffelt & Dearborn (1987), but includes a new parametrization of the degeneracy effects.

The axion emission rate is calculated summing the contributions from the scattering of photons on electrons and ions. We assume that ions are non-degenerate while electrons may have a certain degree of degeneracy. The Coulomb interaction between charges and thermal photons is screened. The typical screening scale is related to the longitudinal component of the polarization tensor which, in the static and non-relativistic limit is (Raffelt 1996)

$$\pi_L = \frac{4Z^2 \alpha m}{\pi} \int_0^\infty \frac{1}{\exp[\beta(E - \mu)] + 1} dp, \quad (\text{A4})$$

where $\beta = 1/k_B T$, with k_B the Boltzmann constant, μ is the chemical potential and $E = m + p^2/2m$ is the fermion energy. In the limit of a non-degenerate plasma, π_L converges to

$$\pi_L \rightarrow \kappa_D^2 = \frac{4\pi Z^2 \alpha n}{T}, \quad (\text{A5})$$

where n is the number density of the charged particles, setting the Debye length as the typical screening scale. For a very degenerate plasma, on the other hand, the relevant screening parameter becomes the Thomas-Fermi scale

$$\pi_L \rightarrow \kappa_{TF}^2 = \frac{4Z^2 \alpha m p_F}{\pi}. \quad (\text{A6})$$

In general, to account for any degree of degeneracy it is convenient to introduce the degeneracy parameter R_{deg} , defined such that

$$\kappa^2 = R_{\text{deg}} \kappa_D^2. \quad (\text{A7})$$

We have derived a good numerical fit for the degeneracy parameter as a function of the temperature and density of the electron gas. Introducing the dimensionless parameter

$$z = \frac{\rho}{T^{3/2} \mu_e}, \quad (\text{A8})$$

where T is in Kelvin and ρ in g cm^{-3} , we find

$$R_{\text{deg}} = 1, \quad (\text{A9})$$

for $z \leq 5.45 \times 10^{-11}$;

$$R_{\text{deg}} = 0.63 + 0.3 \arctan \left(0.65 - 9316 z^{0.48} + \frac{0.019}{z^{0.212}} \right), \quad (\text{A10})$$

for $5.45 \times 10^{-11} < z \leq 7.2 \times 10^{-8}$; and

$$R_{\text{deg}} = 4.78 \times 10^{-6} z^{-0.667}, \quad (\text{A11})$$

for $z > 7.2 \times 10^{-8}$. The precision of the fit is always better than 10%, in the whole region of interest.⁹

A further effect of the partial degeneracy is the reduction of the effective number of targets $n \rightarrow n_{\text{eff}}$, defined, for example, in Raffelt & Dearborn (1987). As shown in Payez et al. (2015), this correction factor is again R_{deg} . Therefore, we find $n_{\text{eff}} = R_{\text{deg}} n$.

We are now ready to provide a numerical recipe for the Primakoff axion production rate. Let us first define the quantities

$$y_{\text{pl}} = \frac{\omega_{\text{pl}}}{T} = \frac{(\rho/\mu_e)^{1/2}}{\left(1 + (1.02 \times 10^{-6} \rho/\mu_e)^{2/3}\right)^{1/4}}, \quad (\text{A12})$$

$$y_{\text{ions}} = 2.57 \times 10^{10} \left(\frac{\rho}{T^3} \sum_{\text{ions}} \frac{Z_j^2 X_j}{A_j} \right)^{1/2}, \quad (\text{A13})$$

$$y_{\text{el}} = 2.57 \times 10^{10} R_{\text{deg}} \left(\frac{\rho}{T^3} \sum_{\text{ions}} \frac{Z_j X_j}{A_j} \right)^{1/2}, \quad (\text{A14})$$

$$y_s = (y_{\text{ions}}^2 + y_{\text{el}}^2)^{1/2} \quad (\text{A15})$$

where T is in K and ρ in g cm^{-3} , and the function

$$f(y_{\text{pl}}, y_s) = \frac{1}{4\pi} \int_{y_{\text{pl}}}^{\infty} \frac{y^2 \sqrt{y^2 - y_{\text{pl}}^2}}{e^y - 1} I(y_{\text{pl}}, y_s) dy. \quad (\text{A16})$$

with

$$I = \frac{r^2 - 1}{s} \ln \left(\frac{r - 1}{r + 1} \right) + \frac{(r + s)^2 - 1}{s} \ln \left(\frac{s + r + 1}{s + r - 1} \right) - 2, \quad (\text{A17})$$

and

$$r = \frac{2y^2 - y_{\text{pl}}^2}{2y\sqrt{y^2 - y_{\text{pl}}^2}}, \quad s = \frac{y_s^2}{2y\sqrt{y^2 - y_{\text{pl}}^2}}. \quad (\text{A18})$$

Therefore, the axion Primakoff emission rate reads

$$\varepsilon = 4.71 \times 10^{-31} g_{10}^2 T^4 \left[\sum_{\text{ions}} (Z_j^2 + R_{\text{deg}} Z_j) \frac{X_j}{A_j} \right] f(y_{\text{pl}}, y_s) \frac{\text{erg}}{\text{g} \cdot \text{s}}, \quad (\text{A19})$$

with $g_{10} = g_{a\gamma}/10^{-10} \text{GeV}^{-1}$ and T in K.

⁹ Notice that this numerical result can be applied only to electrons, not to protons since we used explicitly the electron mass.

A.2. Compton

The Compton axion production, $\gamma + e \rightarrow \gamma + a$, is the production of axions from the scattering of thermal photons on electrons and it is driven by the axion-electron coupling. The non-relativistic cross section is (Raffelt 1996)

$$\sigma = \frac{1}{3} \alpha \left(\frac{g_{ae}}{m_e} \right)^2 \left(\frac{\omega}{m_e} \right)^2, \quad (\text{A20})$$

where ω is the photon energy, assumed to be $\omega \ll m_e$. Here, we have neglected the plasma frequency. This simplification, however, does not substantially modify the result. Additionally, the Compton process is relevant only in the non-degenerate regime since in a degenerate plasma Bremsstrahlung dominates.

The induced energy loss is

$$\varepsilon = R_{\text{deg}} \frac{n_e}{\rho} \int \frac{2 d^3 \mathbf{k}}{(2\pi)^3} \frac{\sigma \omega}{e^{\omega/T} - 1}, \quad (\text{A21})$$

where R_{deg} accounts for the reduction in number of effective electron targets when the plasma is degenerate.¹⁰ We already have a fit for θ_{deg} . Extracting the dependence on ω and setting $x = \omega/T$ we find

$$\varepsilon = R_{\text{deg}} \frac{n_e}{\rho} \frac{8\pi}{(2\pi)^3} \left(\frac{\sigma}{\omega^2} \right) T^6 \int_0^\infty \frac{x^5}{e^x - 1} dx \simeq R_{\text{deg}} \frac{122.1}{3\pi^2} \frac{1}{m_e^4 m_u \mu_e} \alpha g_{ae}^2 T^6. \quad (\text{A22})$$

Numerically:

$$\varepsilon_{\text{compton}} = \theta_{\text{deg}} 2.66 \times 10^{-48} g_{13}^2 \frac{T^6}{\mu_e} \quad (\text{A23})$$

where $g_{13} = g_{ae}/10^{-13}$.

A.3. Bremsstrahlung

The Bremsstrahlung process, $e + Ze \rightarrow e + Ze + a$, is the most important axion production mechanism in a degenerate plasma. Therefore, we will discuss the degenerate limit first. In this limit we neglect the contribution from the scattering on a single electron, since very few electron targets are available in this limit. Additionally, the Debye screening length is a good approximation for the screening length for ions. With these approximations, we find (in units of $\text{erg g}^{-1} \text{s}^{-1}$)

$$\varepsilon_{\text{BD}} = 8.6 F \times 10^{-33} g_{13}^2 T^4 \left(\sum \frac{X_j Z_j^2}{A_j} \right), \quad (\text{A24})$$

where

$$F = \frac{2}{3} \ln \left(\frac{2 + \kappa^2}{\kappa^2} \right) + \left[\frac{2 + 5\kappa^2}{15} \ln \left(\frac{2 + \kappa^2}{\kappa^2} \right) - \frac{2}{3} \right] \beta_F^2, \quad (\text{A25})$$

with

$$\kappa^2 = \frac{k_D^2}{2p_F^2} = 9.27 \times 10^4 \frac{\rho^{1/3}}{T} \left(\sum \frac{X_j Z_j^2}{A_j} \right)^{1/3}, \quad (\text{A26})$$

$$\beta_F = \frac{p_F}{E_F} = \frac{p_F}{\sqrt{m_e^2 + p_F^2}}, \quad (\text{A27})$$

$$p_F = \left(3\pi^2 \frac{\rho}{m_u} \sum \frac{X_j Z_j}{A_j} \right)^{1/3} = 5155 \left(\rho \sum \frac{X_j Z_j}{A_j} \right)^{1/3} \text{ eV}. \quad (\text{A28})$$

In the non-degenerate limit one finds (again, in units of $\text{erg g}^{-1} \text{s}^{-1}$)

$$\varepsilon_{\text{BND}} = 4.7 \times 10^{-25} g_{13}^2 T^{2.5} \frac{\rho}{\mu_e} \sum \frac{X_j Z_j}{A_j} \left(Z_j + \frac{1}{\sqrt{2}} \right). \quad (\text{A29})$$

¹⁰ Notice that the integral can be solved analytically if we neglect ω_{pl} . That is what we do in the following, particularly in Eq. A23. Here we are also ignoring the screening. This is justified since the integral converges (contrarily to what happens in Primakoff and Bremsstrahlung) and so the screening adds only a small correction.

Eq. A29 does not take into account the screening effects, which are always small in the limits of validity of this expression. To take those effects into account, one has to substitute the sum in Eq. A29 with

$$\sum \frac{X_j}{A_j} \left[Z_j^2 \left(1 - \frac{5}{8} \frac{k_S^2}{m_e T} \right) + \frac{Z_j}{\sqrt{2}} \left(1 - \frac{5}{4} \frac{k_S^2}{m_e T} \right) \right] \quad (\text{A30})$$

where k_S accounts for the screening which, in the non-degenerate limit, takes contribution from both electrons and ions. Numerically:

$$\frac{k_S^2}{m_e T} = 1.12 \times 10^{11} \frac{\rho}{T^2} \sum \frac{X_j (Z_j + Z_j^2)}{A_j}. \quad (\text{A31})$$

For the intermediate degeneracy case, we use the approach discussed in Raffelt & Weiss (1995):

$$\varepsilon = \left(\frac{1}{\varepsilon_D} + \frac{1}{\varepsilon_{ND}} \right)^{-1}. \quad (\text{A32})$$

A.4. Pair Production

Finally, axions can be produced from the annihilation of an electron-positron pair, $e^+e^- \rightarrow \gamma + a$. According to Pantziris & Kang (1986), we define the dimensionless parameters

$$\lambda = T/m_e \simeq 1.69 \times 10^{-10} T_K, \quad (\text{A33})$$

and

$$\nu = \mu/T, \quad (\text{A34})$$

and distinguish among different plasma conditions.

In the non-degenerate and non-relativistic regime, we find

$$\varepsilon = \frac{g_{ae}^2 \alpha}{4\pi^3 \rho} m_e^2 T^3 e^{-2/\lambda} \left(1 + \frac{\lambda}{2} \right). \quad (\text{A35})$$

The degenerate case is given in Pantziris & Kang (1986) and applies to the case of $\lambda \ll 1$ and $1/\lambda \ll \nu \ll 2/\lambda$. The result is cumbersome

$$\varepsilon = \frac{g_{ae}^2 \alpha}{\pi^4 \rho} m_e^2 T^3 e^\eta \int_0^\infty \frac{dx \sqrt{x}}{e^{x-a} + 1} \int_0^\infty \frac{dy \sqrt{y}}{e^y} \left(1 + \frac{x+y}{6} \lambda \right), \quad (\text{A36})$$

where $\eta = \nu - 1/\lambda$.¹¹ A simplified expression, accurate to about 15% in the whole range of interest, is

$$\varepsilon = \frac{g_{ae}^2 \alpha}{\pi^4 \rho} m_e^2 T^3 e^{\nu-1/\lambda} f(\nu - 1/\lambda), \quad (\text{A37})$$

where

$$f(x) = 0.605 e^{-0.84x}. \quad (\text{A38})$$

Finally, in the non-relativistic and mildly degenerate case ($\mu \simeq m_e$), we find the expression

$$\varepsilon = \frac{g_{ae}^2 \alpha}{4\pi^3 \rho} m_e^2 T^3 e^{-2/\lambda} 0.76 (1 + 0.53\lambda). \quad (\text{A39})$$

A numerical expression for the axion pair production in cgs units that summarizes all the previous results is

$$\varepsilon = \frac{2.14 \times 10^{16} g_{13}^2 \lambda^3}{\rho} \frac{\text{erg}}{\text{g s}} e^{-\text{Max}(\eta, 0) - 2/\lambda} F, \quad (\text{A40})$$

where F is

¹¹ Notice that, in the limit of validity of this approximation, $\eta < 1/\lambda$.

- Non degenerate:

$$F = \frac{1}{4} \left(1 + \frac{\lambda}{2} \right); \quad (\text{A41})$$

- Mildly degenerate:

$$F = 0.19 (1 + 0.53\lambda); \quad (\text{A42})$$

- Degenerate:

$$F = \frac{1}{\pi} f(\eta). \quad (\text{A43})$$

REFERENCES

- Aalbers, J., et al. 2016, JCAP, 1611, 017
- Abbott, L. F., & Sikivie, P. 1983, Phys. Lett., B120, 133, [URL(1982)]
- Akerib, D. S., et al. 2017, Phys. Rev. Lett., 118, 261301
- Alesini, D., Babusci, D., Di Gioacchino, D., et al. 2017, arXiv e-prints, arXiv:1707.06010
- Alexander, D. R., & Ferguson, J. W. 1994, ApJ, 437, 879
- Anastassopoulos, V., et al. 2017, Nature Phys., 13, 584
- Aprile, E., Agostini, F., Alfonsi, M., et al. 2014, PhRvD, 90, 062009
- Arias, P., Cadamuro, D., Goodsell, M., et al. 2012, JCAP, 1206, 013
- Armengaud, E., et al. 2014, JINST, 9, T05002
- . 2019, arXiv e-prints, arXiv:1904.09155
- Arvanitaki, A., Dimopoulos, S., Dubovsky, S., Kaloper, N., & March-Russell, J. 2010, Phys. Rev., D81, 123530
- Ayala, A., Domínguez, I., Giannotti, M., Mirizzi, A., & Straniero, O. 2014, Physical Review Letters, 113, 191302
- Barbarino, C., Dall’Ora, M., Botticella, M. T., et al. 2015, MNRAS, 448, 2312
- Beaudet, G., Petrosian, V., & Salpeter, E. E. 1967, ApJ, 150, 979
- Bechtol, K., et al. 2019, arXiv e-prints, arXiv:1903.04425
- Beda, A. G., Brudanin, V. B., Egorov, V. G., et al. 2013, Physics of Particles and Nuclei Letters, 10, 139
- Bhre, R., et al. 2013, JINST, 8, T09001
- Brubaker, B. M., Zhong, L., Lamoreaux, S. K., Lehnert, K. W., & van Bibber, K. A. 2017, Phys. Rev., D96, 123008
- Brun, P., et al. 2019, Eur. Phys. J., C79, 186
- Caughlan, G. R., & Fowler, W. A. 1988, Atomic Data and Nuclear Data Tables, 40, 283
- Chieffi, A., & Straniero, O. 1989, ApJS, 71, 47
- Conlon, J. P. 2006, JHEP, 05, 078
- Córsico, A. H., Romero, A. D., Althaus, L. G., et al. 2016, JCAP, 7, 036
- Cox, J. P., & Giuli, R. T. 1968, Principles of stellar structure (New York: Gordon and Breach)
- Davies, B., & Beasor, E. R. 2018, MNRAS, 474, 2116
- deBoer, R. J., Görres, J., Wiescher, M., et al. 2017, Rev. Mod. Phys., 89, 035007. <https://link.aps.org/doi/10.1103/RevModPhys.89.035007>
- Dewitt, H. E., Graboske, H. C., & Cooper, M. S. 1973, ApJ, 181, 439
- Di Luzio, L., Mescia, F., & Nardi, E. 2016, arXiv e-prints, arXiv:1610.07593
- Di Vecchia, P., Giannotti, M., Lattanzi, M., & Lindner, A. 2019, in 13th Conference on Quark Confinement and the Hadron Spectrum (Confinement XIII) Maynooth, Ireland, July 31-August 6, 2018
- Dicus, D. A., Kolb, E. W., Schramm, D. N., & Tubbs, D. L. 1976, ApJ, 210, 481
- Dine, M., & Fischler, W. 1983, Phys. Lett., B120, 137, [URL(1982)]
- Dine, M., Fischler, W., & Srednicki, M. 1981, Physics Letters B, 104, 199
- Dominguez, I., Straniero, O., & Isern, J. 1999, Mon. Not. Roy. Astron. Soc., 306, 1
- Drlica-Wagner, A., et al. 2019, arXiv e-prints, arXiv:1902.01055
- Du, N., et al. 2018, Phys. Rev. Lett., 120, 151301
- Ebinger, K., Curtis, S., Fröhlich, C., et al. 2019, ApJ, 870, 1
- Eggenberger, P., Deheuvels, S., Miglio, A., et al. 2019, A&A, 621, A66
- Eldridge, J. J., Izzard, R. G., & Tout, C. A. 2008, MNRAS, 384, 1109
- Eldridge, J. J., & Tout, C. A. 2004, MNRAS, 353, 87
- Endal, A. S., & Sofia, S. 1976, ApJ, 210, 184
- Ertl, T., Janka, H.-T., Woosley, S. E., Sukhbold, T., & Ugliano, M. 2016, ApJ, 818, 124
- Farmer, R., Fields, C. E., Petermann, I., et al. 2016, ApJS, 227, 22
- Freytag, B., Ludwig, H.-G., & Steffen, M. 1996, A&A, 313, 497
- Friedland, A., Giannotti, M., & Wise, M. 2013, Phys. Rev. Lett., 110, 061101

- Fu, C., et al. 2017, *Phys. Rev. Lett.*, 119, 181806
- Fuller, J. 2017, *MNRAS*, 470, 1642
- Fynbo, H. O. U., Diget, C. A., Bergmann, U. C., et al. 2005, *Nature*, 433, 136
- Georgy, C., Ekström, S., Eggenberger, P., et al. 2013, *A&A*, 558, A103
- Giannotti, M. 2015, in *Proceedings, 11th Patras Workshop on Axions, WIMPs and WISPs (Axion-WIMP 2015): Zaragoza, Spain, June 22-26, 2015*, 26–30
- Giannotti, M., Irastorza, I., Redondo, J., & Ringwald, A. 2016a, *JCAP*, 1605, 057
- Giannotti, M., Ruz, J., & Vogel, J. K. 2016b, *PoS, ICHEP2016*, 195
- Goriely, S., Hilaire, S., & Koning, A. J. 2008, *A&A*, 487, 767
- Graboske, H. C., Dewitt, H. E., Grossman, A. S., & Cooper, M. S. 1973, *ApJ*, 181, 457
- Haft, M., Raffelt, G., & Weiss, A. 1994, *ApJ*, 425, 222
- Heger, A., Friedland, A., Giannotti, M., & Cirigliano, V. 2009, *ApJ*, 696, 608
- Heger, A., & Langer, N. 2000, *ApJ*, 544, 1016
- Hirschi, R., Meynet, G., & Maeder, A. 2004, *A&A*, 425, 649
- Horiuchi, S., Nakamura, K., Takiwaki, T., Kotake, K., & Tanaka, M. 2014, *MNRAS*, 445, L99
- Hunter, I., Lennon, D. J., Dufton, P. L., et al. 2008, *A&A*, 479, 541
- Hunter, I., Brott, I., Langer, N., et al. 2009, *A&A*, 496, 841
- Iglesias, C. A., & Rogers, F. J. 1996, *ApJ*, 464, 943
- Imbriani, G., Limongi, M., Gialanella, L., et al. 2001, *ApJ*, 558, 903
- Irastorza, I. G., & Redondo, J. 2018, *Progress in Particle and Nuclear Physics*, 102, 89
- Isern, J., García-Berro, E., Torres, S., Cojocaru, R., & Catalán, S. 2018, *MNRAS*, 478, 2569
- Itoh, N., Hayashi, H., Nishikawa, A., & Kohyama, Y. 1996a, *ApJS*, 102, 411
- Itoh, N., Nishikawa, A., & Kohyama, Y. 1996b, *ApJ*, 470, 1015
- Itoh, N., Totsuji, H., Ichimaru, S., & Dewitt, H. E. 1979, *ApJ*, 234, 1079
- Jerkstrand, A., Smartt, S. J., Fraser, M., et al. 2014, *MNRAS*, 439, 3694
- Jiang, C. L., Rehm, K. E., Back, B. B., & Janssens, R. V. F. 2007, *PhRvC*, 75, 015803
- Kim, J. E. 1979, *Physical Review Letters*, 43, 103
- Kippenhahn, R. 1974, in *IAU Symposium, Vol. 66, Late Stages of Stellar Evolution*, ed. R. J. Tayler & J. E. Hesser, 20
- Kippenhahn, R., & Weigert, A. 1990, *Stellar Structure and Evolution (Springer-Verlag Berlin Heidelberg New York. Also Astronomy and Astrophysics Library)*, 468
- Krishna Swamy, K. S. 1966, *ApJ*, 145, 174
- Kunz, R., Fey, M., Jaeger, M., et al. 2002, *ApJ*, 567, 643
- Langer, N., El Eid, M. F., & Fricke, K. J. 1985, *A&A*, 145, 179
- Limongi, M., & Chieffi, A. 2018, *ApJS*, 237, 13
- Limongi, M., Straniero, O., & Chieffi, A. 2000, *ApJS*, 129, 625
- Lodders, K., Palme, H., & Gail, H.-P. 2009, *Landolt Börnstein*, 712
- Maeder, A. 2009, *Physics, Formation and Evolution of Rotating Stars (Astronomy and Astrophysics Library. Springer Berlin Heidelberg)*, doi:10.1007/978-3-540-76949-1
- Maeder, A., & Meynet, G. 1989, *A&A*, 210, 155
- Magee, N. H., Abdallah, Jr., J., Clark, R. E. H., et al. 1995, in *Astronomical Society of the Pacific Conference Series, Vol. 78, Astrophysical Applications of Powerful New Databases*, ed. S. J. Adelman & W. L. Wiese, 51
- Meynet, G., Chomienne, V., Ekström, S., et al. 2015, *A&A*, 575, A60
- Miller Bertolami, M. M., Melendez, B. E., Althaus, L. G., & Isern, J. 2014, *JCAP*, 10, 069
- Mohr, P. J., Newell, D. B., & Taylor, B. N. 2016, *Journal of Physical and Chemical Reference Data*, 45, 043102. <https://doi.org/10.1063/1.4954402>
- Moriya, T., Tominaga, N., Blinnikov, S. I., Baklanov, P. V., & Sorokina, E. I. 2011, *MNRAS*, 415, 199
- Morozova, V., Piro, A. L., & Valenti, S. 2017, *ApJ*, 838, 28
- . 2018, *ApJ*, 858, 15
- Mukhamedzhanov, A. M., & Pang, D. Y. 2018, *arXiv e-prints*, arXiv:1806.08828
- Nieuwenhuijzen, H., & de Jager, C. 1990, *A&A*, 231, 134
- Nomoto, K., Iwamoto, K., & Suzuki, T. 1995, *Physics Reports*, 256, 173, the Physics of Supernovae. <http://www.sciencedirect.com/science/article/pii/037015739400107E>
- O'Connor, E., & Ott, C. D. 2011, *ApJ*, 730, 70
- Paczyński, B. 1967, *AcA*, 17, 193
- Pagel, B. E. J., & Portinari, L. 1998, *MNRAS*, 298, 747
- Pantziris, A., & Kang, K. 1986, *Phys. Rev.*, D33, 3509
- Payez, A., Evoli, C., Fischer, T., et al. 2015, *JCAP*, 1502, 006
- Peccei, R. D., & Quinn, H. R. 1977, *Physical Review Letters*, 38, 1440
- Pejcha, O., & Thompson, T. A. 2015, *ApJ*, 801, 90
- Piersanti, L., Cristallo, S., & Straniero, O. 2013, *ApJ*, 774, 98

- Piersanti, L., Straniero, O., & Cristallo, S. 2007, *A&A*, 462, 1051
- Podsiadlowski, P., Joss, P. C., & Hsu, J. J. L. 1992, *ApJ*, 391, 246
- Potekhin, A. Y. 1999, *A&A*, 351, 787
- Potekhin, A. Y., Baiko, D. A., Haensel, P., & Yakovlev, D. G. 1999, *A&A*, 346, 345
- Prada Moroni, P. G., & Straniero, O. 2002, *ApJ*, 581, 585
- Preskill, J., Wise, M. B., & Wilczek, F. 1983, *Phys. Lett.*, B120, 127, [URL(1982)]
- Raffelt, G., & Weiss, A. 1995, *Phys. Rev.*, D51, 1495
- Raffelt, G. G. 1986, *Phys.Rev.*, D33, 897
- Raffelt, G. G. 1996, *Stars as laboratories for fundamental physics : the astrophysics of neutrinos, axions, and other weakly interacting particles* (University of Chicago Press, QB464.2 .R34 1996)
- Raffelt, G. G. 2008, *Lect. Notes Phys.*, 741, 51, [51(2006)]
- Raffelt, G. G., & Dearborn, D. S. 1987, *Phys.Rev.*, D36, 2211
- Ringwald, A. 2012, *Phys. Dark Univ.*, 1, 116
- Rogers, F. J., Swenson, F. J., & Iglesias, C. A. 1996, *ApJ*, 456, 902
- Sallaska, A. L., Iliadis, C., Champagne, A. E., et al. 2013, *ApJS*, 207, 18
- Sana, H., de Mink, S. E., de Koter, A., et al. 2012, *Science*, 337, 444
- Shifman, M. A., Vainshtein, A. I., & Zakharov, V. I. 1980, *Nuclear Physics B*, 166, 493
- Smartt, S. J. 2009, *ARA&A*, 47, 63
- . 2015, *PASA*, 32, e016
- Spiro, S., Pastorello, A., Pumo, M. L., et al. 2014, *MNRAS*, 439, 2873
- Stothers, R. B., & Chin, C.-W. 1992a, *ApJL*, 390, L33
- . 1992b, *ApJ*, 390, 136
- . 1994, *ApJ*, 431, 797
- Straniero, O. 1988, *A&AS*, 76, 157
- Straniero, O., Ayala, A., Giannotti, M., Mirizzi, A., & Dominguez, I. 2015, in *Proceedings, 11th Patras Workshop on Axions, WIMPs and WISPs (Axion-WIMP 2015): Zaragoza, Spain, June 22-26, 2015*, 77–81
- Straniero, O., Dominguez, I., Giannotti, M., & Mirizzi, A. 2018, in *Proceedings, 13th Patras Workshop on Axions, WIMPs and WISPs, (PATRAS 2017): Thessaloniki, Greece, 15 May 2017 - 19, 2017*, 172–176
- Straniero, O., Domínguez, I., Imbriani, G., & Piersanti, L. 2003, *ApJ*, 583, 878
- Straniero, O., Gallino, R., & Cristallo, S. 2006, *Nuclear Physics A*, 777, 311
- Straniero, O., Piersanti, L., & Cristallo, S. 2016, in *Journal of Physics Conference Series, Vol. 665, Journal of Physics Conference Series*, 012008
- Straniero, O., Piersanti, L., Dominguez, I., & Tumino, A. 2019, *arXiv e-prints*, arXiv:1901.00173
- Sukhbold, T., Ertl, T., Woosley, S. E., Brown, J. M., & Janka, H.-T. 2016, *ApJ*, 821, 38
- Sukhbold, T., Woosley, S. E., & Heger, A. 2018, *ApJ*, 860, 93
- Svrcek, P., & Witten, E. 2006, *JHEP*, 06, 051
- Tumino, A., Spitaleri, C., La Cognata, M., et al. 2018, *Nature*, 557, 687
- Ugliko, M., Janka, H.-T., Marek, A., & Arcones, A. 2012, *ApJ*, 757, 69
- Utrobin, V. P., & Chugai, N. N. 2009, *A&A*, 506, 829
- Valenti, S., Howell, D. A., Stritzinger, M. D., et al. 2016, *MNRAS*, 459, 3939
- Vanbeveren, D., De Loore, C., & Van Rensbergen, W. 1998, *The Astronomy and Astrophysics Review*, 9, 63. <https://doi.org/10.1007/s001590050015>
- Viaux, N., Catelan, M., Stetson, P. B., et al. 2013a, *A&A*, 558, A12
- . 2013b, *Physical Review Letters*, 111, 231301
- Weaver, T. A., & Woosley, S. E. 1993, *PhR*, 227, 65
- Weinberg, S. 1978, *Physical Review Letters*, 40, 223
- Wilczek, F. 1978, *Physical Review Letters*, 40, 279
- Witten, E. 1984, *Phys. Lett.*, 149B, 351
- Woosley, S. E., & Heger, A. 2007, *PhR*, 442, 269
- Woosley, S. E., Heger, A., & Weaver, T. A. 2002, *Reviews of Modern Physics*, 74, 1015
- Yaron, O., Perley, D. A., Gal-Yam, A., et al. 2017, *Nature Physics*, 13, 510
- Yoon, S. C., Woosley, S. E., & Langer, N. 2010, *ApJ*, 725, 940
- Zhitnitskii, A. P. 1980, *Soviet Journal of Nuclear Physics*, 31, 260
- Zickefoose, J., Di Leva, A., Strieder, F., et al. 2018, *PhRvC*, 97, 065806